

AD-A102 522 MISSION RESEARCH CORP SANTA BARBARA CA F/G 4/1
EXCEDE ENERGY DEPOSITION. THEORY AND EXPERIMENT COMPARED.(U)
NOV 80 D H ARCHER DNA001-79-C-0116
UNCLASSIFIED MRC-R-599 DNA-5525F NL

1 OF 1
AND
02602

END
DATE
FILMED
8-8
DTIC

LEVEL *IV*



DNA 5525F

EXCEDE ENERGY DEPOSITION

Theory and Experiment Compared

Douglas H. Archer
Mission Research Corporation
P.O. Drawer 719
Santa Barbara, California 93102

30 November 1980

Final Report for Period 31 October 1979—31 October 1980

CONTRACT No. DNA 001-79-C-0116

APPROVED FOR PUBLIC RELEASE;
DISTRIBUTION UNLIMITED.

THIS WORK SPONSORED BY THE DEFENSE NUCLEAR AGENCY
UNDER RDT&E RMSS CODE B323079464 S99QAXH100430 H2590D.

Prepared for
Director
DEFENSE NUCLEAR AGENCY
Washington, D. C. 20305

81 8 05 018

AD A102522

DTIC FILE COPY



Destroy this report when it is no longer
needed. Do not return to sender.

PLEASE NOTIFY THE DEFENSE NUCLEAR AGENCY,
ATTN: STTI, WASHINGTON, D.C. 20305, IF
YOUR ADDRESS IS INCORRECT, IF YOU WISH TO
BE DELETED FROM THE DISTRIBUTION LIST, OR
IF THE ADDRESSEE IS NO LONGER EMPLOYED BY
YOUR ORGANIZATION.



UNCLASSIFIED

SECURITY CLASSIFICATION OF THIS PAGE (When Data Entered)

REPORT DOCUMENTATION PAGE		READ INSTRUCTIONS BEFORE COMPLETING FORM
1 REPORT NUMBER DNA 5525F ✓	2 GOVT ACCESSION NO. AD-A102522	3 RECIPIENT'S CATALOG NUMBER
4 TITLE (and Subtitle) EXCEDE ENERGY DEPOSITION. Theory and Experiment Compared.	5 TYPE OF REPORT & PERIOD COVERED Final Report, for Period 31 Oct 79 - 31 Oct 80, 1	6 PERFORMING ORG. REPORT NUMBER MRC-R-599 ✓
7 AUTHOR Douglas H. Archer	8 CONTRACT OR GRANT NUMBER(s) DNA 001-79-C-0116	
9 PERFORMING ORGANIZATION NAME AND ADDRESS Mission Research Corporation P.O. Drawer 719 Santa Barbara, California 93102	10 PROGRAM ELEMENT PROJECT TASK AREA & WORK UNIT NUMBERS Subtask S99QAXHI004-30	
11 CONTROLLING OFFICE NAME AND ADDRESS Director Defense Nuclear Agency Washington, D.C. 20305	12 REPORT DATE 30 November 1980	
14 MONITORING AGENCY NAME & ADDRESS (if different from Controlling Office)	13 NUMBER OF PAGES 62	
	15 SECURITY CLASS (of this report) UNCLASSIFIED	
	15a DECLASSIFICATION DOWNGRADING SCHEDULE N/A	
16 DISTRIBUTION STATEMENT (of this Report) Approved for public release; distribution unlimited.		
17 DISTRIBUTION STATEMENT (of the abstract entered in Block 20, if different from Report)		
18 SUPPLEMENTARY NOTES This work sponsored by the Defense Nuclear Agency under RDT&E RMSS Code B323079464 S99QAXHI00430 H2590D.		
19 KEY WORDS (Continue on reverse side if necessary and identify by block number) Electron beams Electron deposition EXCEDE		
20 ABSTRACT (Continue on reverse side if necessary and identify by block number) This report describes work performed to determine the adequacy of code calculations (based on single particle deposition in ambient air) to describe the energy deposition rate surrounding electron beams at E-region altitudes in the atmosphere. Comparisons are made between model predictions and camera data from the PRECEDE II and EXCEDE:SPECTRAL experiments. Large discrepancies are found to exist between theory and experiment, at least for the EXCEDE:SPECTRAL event, in the region near the electron accelerator. The discrepancies are tentatively		

DD FORM 1 JAN 73 1473

EDITION OF 1 NOV 65 IS OBSOLETE

UNCLASSIFIED

SECURITY CLASSIFICATION OF THIS PAGE (When Data Entered)

UNCLASSIFIED

SECURITY CLASSIFICATION OF THIS PAGE(When Data Entered)

20. ABSTRACT (continued)

attributed to a beam plasma discharge effect that is not described by the standard theory. Recommendations are made for work to help clarify the phenomenon.

UNCLASSIFIED

SECURITY CLASSIFICATION OF THIS PAGE(When Data Entered)

TABLE OF CONTENTS

Section		Page
	LIST OF ILLUSTRATIONS	2
1	INTRODUCTION	5
2	PRECEDE/EXCEDE CALCULATIONS	6
	PRELIMINARY	6
	ENERGY DEPOSITION BY 3-KEV ELECTRON BEAM	9
	COMPARISON WITH PRECEDE II IMAGE	23
3	EXCEDE:SPECTRAL CALCULATIONS	35
	PRELIMINARY	35
	CODE CALCULATIONS AND COMPARISONS WITH PHOTOMETRICS DATA	36
	COMPARISON WITH PRELIMINARY TIC DATA	47
	COMMENTS	48
4	SUMMARY, CONCLUSIONS, AND RECOMMENDATIONS	51
	REFERENCES	54

Accession For	
NTIS GRA&I	<input checked="" type="checkbox"/>
DTIC TAB	<input type="checkbox"/>
Unannounced	<input type="checkbox"/>
Justification	
By	
Distribution/	
Availability Codes	
Avail and/or	
Dist Special	

A

LIST OF ILLUSTRATIONS

Figure		Page
2-1.	Ratio of electron mean free path to Larmour radius.	8
2-2.	Volume deposition rate of 3-keV electron beam in earth's magnetic field in normalized units for current of 1 electron/sec, $\theta_0 = 0^\circ$.	10
2-3.	Volume deposition rate of 3-keV beam in earth's magnetic field in normalized units for current of 1 electron/sec, $\theta_0 = 88^\circ$.	11
2-4.	Contours of normalized brightness perpendicular to earth's magnetic field for a current of 1 electron/sec, $\theta_0 = 0^\circ$.	12
2-5.	Contours of normalized brightness perpendicular to earth's magnetic field for a current of 1 electron/sec, $\theta_0 = 15^\circ$.	13
2-6.	Contours of normalized brightness perpendicular to earth's magnetic field for a current of 1 electron/sec, $\theta_0 = 30^\circ$.	14
2-7.	Contours of normalized brightness perpendicular to earth's magnetic field for a current of 1 electron/sec, $\theta_0 = 45^\circ$.	15
2-8.	Contours of normalized brightness perpendicular to earth's magnetic field for a current of 1 electron/sec, $\theta_0 = 60^\circ$.	16
2-9.	Contours of normalized brightness perpendicular to earth's magnetic field for a current of 1 electron/sec, $\theta_0 = 65^\circ$.	17
2-10.	Contours of normalized brightness perpendicular to earth's magnetic field for a current of 1 electron/sec, $\theta_0 = 75^\circ$.	18
2-11.	Contours of normalized brightness perpendicular to earth's magnetic field for a current of 1 electron/sec, $\theta_0 = 80^\circ$.	19

LIST OF ILLUSTRATIONS (continued)

Figure		Page
2-12.	Contours of normalized brightness perpendicular to earth's magnetic field for a current of 1 electron/sec, $\theta_0 = 85^\circ$.	20
2-13.	Contours of normalized brightness perpendicular to earth's magnetic field for a current of 1 electron/sec, $\theta_0 = 88^\circ$.	21
2-14.	Contours of normalized brightness perpendicular to earth's magnetic field for a current of 1 electron/sec, $\theta_0 = 90^\circ$.	22
2-15.	Column deposition rate, for a single electron, parallel to the earth's field, for parametric values of the electron's initial pitch angle.	24
2-16.	Column deposition rate, for a single electron, normal to the earth's field, for parametric values of the electron's initial pitch angle.	25
2-17.	Column deposition rate, for a single electron, normal to the earth's field, for parametric values of the electron's initial pitch angle.	26
2-18.	PRECEDE II experiment: White Sands missile range map (from Reference 2-2).	27
2-19.	PRECEDE II geometry.	29
2-20.	Calculated brightness at 3914 Å normal to magnetic field as function of distance along central field line for three electron pitch angles.	30
2-21.	Calculated brightness at 3914 Å normal to magnetic field along line through electron gun.	32
2-22.	Projection of PRECEDE II image at 102.3-km altitude in magnetic meridian plane compared with calculated images for 65° and 80° pitch angles and radial diameter of 70 meters.	33
3-1.	Plan view of the projection of the cameras' field of view and the region into which electrons from EXCEDE: SPECTRAL accelerator #4 deposit energy (as measured by the cameras) (from Reference 3-1).	37

LIST OF ILLUSTRATIONS (continued)

Figure		Page
3-2.	Volume deposition rate (eV gm^{-1}) of 3-keV electron beam in earth's magnetic field in normalized units for current of 1 electron/sec, beam initially parallel with 0° pitch angle.	38
3-3.	Volume deposition rate (eV gm^{-1}) of 3-keV electron beam in earth's magnetic field in normalized units for current of 1 electron/sec; beam initially in cone of semi angle 15° with axis parallel to magnetic field.	39
3-4.	"In-band" radiance distribution projected to the onboard camera when EXCEDE:SPECTRAL is at 123 km and the outboard electron accelerator (#4 in Figure 3-1) emits 7 amperes.	41
3-5.	Calculated radiance (3914 \AA) distribution in image plane of camera (corresponding to Figure 3-4) if electron beam were initially parallel with 0° pitch angle.	42
3-6.	Calculated radiance (3914 \AA) distribution in image plane of camera (corresponding to Figure 3-4) for the case where the electron beam is initially in a cone of semi angle 15° with cone axis parallel to the earth's field.	43
3-7.	EXCEDE:SPECTRAL radiance projected to the onboard camera along the electron beam axis and also viewing perpendicular to the axis; calculation and photographic data compared.	45
3-8.	Radiance projected to the onboard camera transverse to the electron beam's axis. Solid curves are "in-band" data from Ref. 3-1; dotted curves are calculated values for 3914 \AA .	46
3-9.	EXCEDE:SPECTRAL radiance (3914 \AA) normal to beam axis at 124 km (ascent); calculation and photographic data compared.	49

SECTION 1 INTRODUCTION

This report presents the results of work relating to the DNA infrared field program performed under Contract DNA 001-79-C-001. Other work, performed under the same contract, dealing with recommendations for improving our LWIR prediction capability for a nuclear environment, was reported separately in Mission Research Corporation report MRC-R-585 (Reference 1-1).

Section 2 describes calculations performed to determine the spatial distribution of the energy deposition rate produced in the upper atmosphere by the injection of 3-keV electron beams incident at various pitch angles to the earth's magnetic field, and the resultant brightness at 3914 \AA from excitation of the N_2^+ First Negative (0-0) band. Contours of constant brightness, viewing normal to the electron beam, are obtained and are used in making comparisons with the profile of a video image recorded from the ground near White Sands, New Mexico during the PRECEDE II event.

Section 3 reports the preliminary results of a comparison made between calculations of the 3914 \AA brightness from a 3-kV, 7-A electron beam at an altitude of 125 km and reduced photographic data from an image recorded by a camera on board the EXCEDE:SPECTRAL rocket over Poker Flat, Alaska. The significant differences between theory and experiment are discussed.

Section 4 is an overall summary of the results and conclusions in the previous two sections, and presents recommendations for work to help clarify the apparent anomalous behavior of electron beams in EXCEDE experiments.

SECTION 2

PRECEDE/EXCEDE CALCULATIONS

PRELIMINARY

The EXCEDE experiments, in which observations are made of the optical/infrared (IR) and ionization effects of energy deposition in the atmosphere by beams of kilovolt electrons, have been carried out by the Air Force Geophysics Laboratory (AFGL) for DNA in the past few years. The ionization levels and deposition rates achieved in these experiments approximately simulate those of a high-altitude nuclear detonation, albeit over a much more confined volume of space. Calculation of the IR emission from the dosed regions proceeds in a manner analogous to that for a nuclear detonation, the calculation in both cases starting from the spatial distribution of prompt energy deposition. Comparison between the calculated and observed emissions in these experiments should serve as an important aid in determining the validity of our calculational techniques for a nuclear environment. The purpose of the work reported in this section is twofold. First, to attempt to verify the first step in such a calculation, namely, the prompt energy deposition surrounding the electron gun.* Second, to provide energy deposition contours as an aid in planning future EXCEDE-type experiments.

* A portion of this work was supported under Subcontract 78-045 from Utah State University, under the auspices of AFGL.

The basis for the present work is described in Reference 2-1. In that report, the theory of electron deposition in a magnetic field was developed and a code for determining the spatial distribution of energy deposited about an electron gun in the atmosphere was subsequently constructed. The theory, embodied in the code, is applicable when the electron mean free path, λ , is at least twice the Larmour radius, R_L . Under these conditions, the magnetic field provides the main symmetry and controls the radial dispersion of the deposition which is then independent of altitude. In the opposite limit, $\lambda/R_L \ll 1$, the magnetic field is unimportant, deposition symmetry is about the beam axis, and the radial dispersion is altitude dependent. An altitude plot of λ/R_L , for selected values of the initial electron energy, is shown in Figure 2-1. From this figure we see that for a 3 keV beam (which is characteristic of the EXCEDE experiments) the code should be applicable at altitudes above about 94 km.

In Reference 2-1, sample results are shown for a 3-keV electron beam incident, initially, at various pitch angles, θ_0 , to the earth's magnetic field. Included are contour plots of the volume deposition rate in scaled units (eV/gm) as functions of the radial distance (meters) from the central guiding field line and distance (gm/cm^2) along the field line from the electron gun nozzle. In the present work, we have gone beyond these calculations by (1) extending the spatial region over which the calculations are performed by approximately a factor of 2 in both along-the-field and normal-to-the-field directions, (2) performing the calculations for different electron pitch angles, and (3) providing contours of brightness (column deposition rate) normal to the earth's field.

The results of these calculations are presented below together with a detailed comparison between a calculated and observed image from the PRECEDE II event.

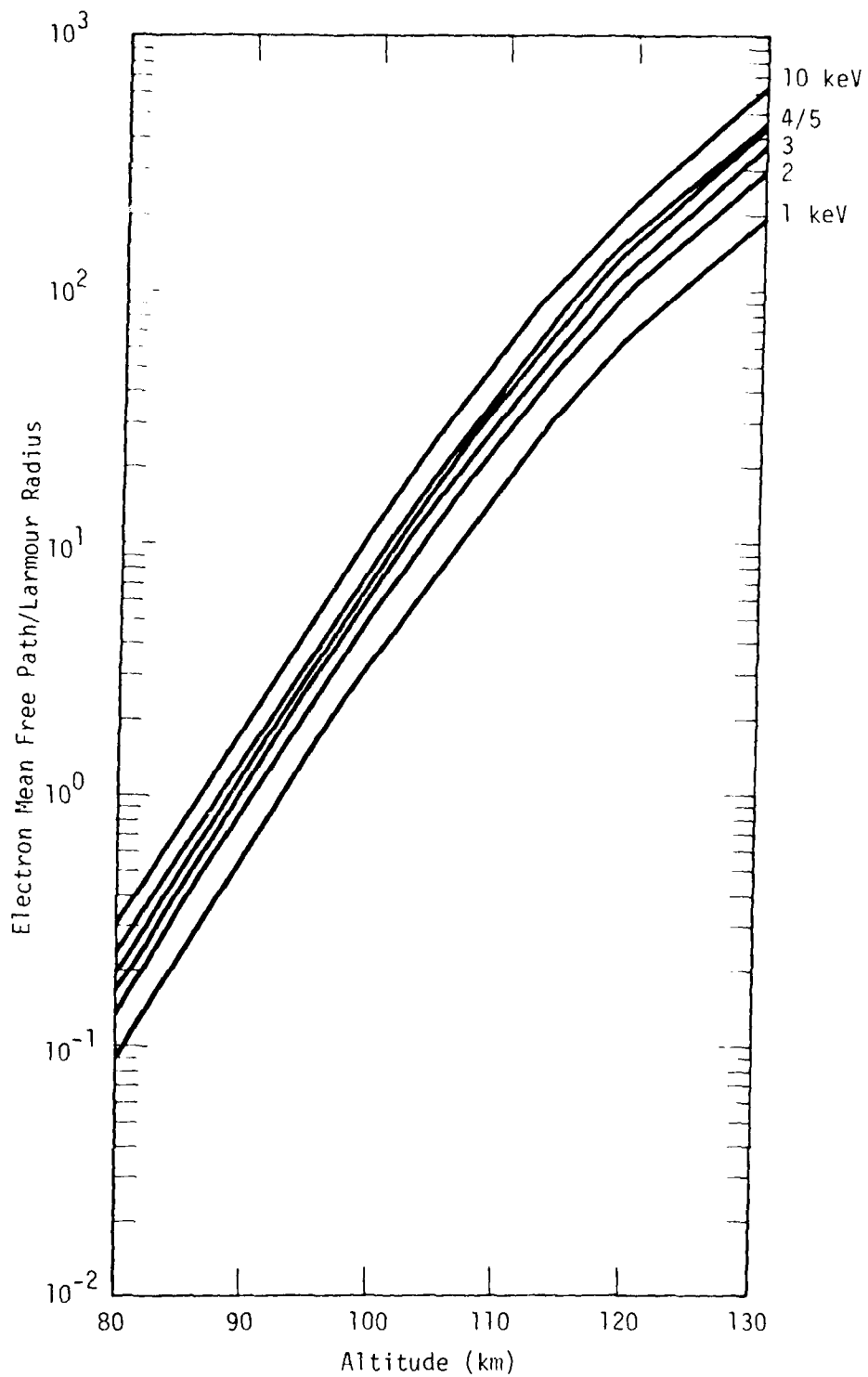


Figure 2-1. Ratio of electron mean free path to Larmour radius.

ENERGY DEPOSITION BY 3-KEV ELECTRON BEAM

The electron beam deposition code has been run to obtain results relating to the spatial distribution of energy about 3-keV beams for parametric values of the initial electron pitch angle θ_0 . The key quantity calculated is the volume deposition rate, $d\epsilon/dt$, from which other useful quantities can be determined. In Reference 2-1, normalized volume deposition rate contours for a single 3-keV electron were presented for pitch angles between 0° and 90° incremented by 15° . Those calculations were repeated for a larger deposition volume and augmented by additional calculations for pitch angles 65° , 80° , 85° , and 88° . Figures 2-2 and 2-3 show sample results for $\theta_0 = 0^\circ$ and 88° , respectively. In these figures, the ordinate, R , is the distance (meters) along a normal to the initial guiding field line, the abscissa, Z , is the distance (gm cm^{-2}) along the initial guiding field line measured from the gun exit. Deposition at negative values for Z arises from electron scattering. The contour values are in units of eV gm^{-1} but they can be converted to units of $\text{eV cm}^{-3} \text{ sec}^{-1}$ by multiplying by $6.25 \times 10^{18} I \rho$, where I is the current in amperes and ρ is the local density in gm cm^{-3} . The distance, Z , parallel to the field can be converted to units of cm by dividing by ρ .

Figures 2-4 through 2-14 show contours of constant brightness (column deposition rate) viewing normal to the field lines for a single 3-keV electron incident, initially, at selected pitch angles, θ_0 , to the earth's field. The ordinate, D , is the perpendicular distance (meters) from the initial guiding field line and the abscissa, Z , is again the distance (gm cm^{-2}) along the field from the gun exit. To convert to real space, divide Z by ρ , and to convert the contour values, in units of eV cm gm^{-1} , to units of $\text{eV cm}^{-2} \text{ sec}^{-1}$, multiply by $6.25 \times 10^{18} I \rho$. The contour values can be converted to units of kilorayleighs (kR) of 3914 Å emissions as follows:*

$$\text{kR}(3914 \text{ Å}) = 8.9 \times 10^6 I(\text{amps}) \rho(\text{gm cm}^{-3}) \times \text{Contour Value}$$

* This conversion assumes a fluorescence efficiency for the N_2^+ First Negative emission at 3914 Å of 4.5×10^{-5} .

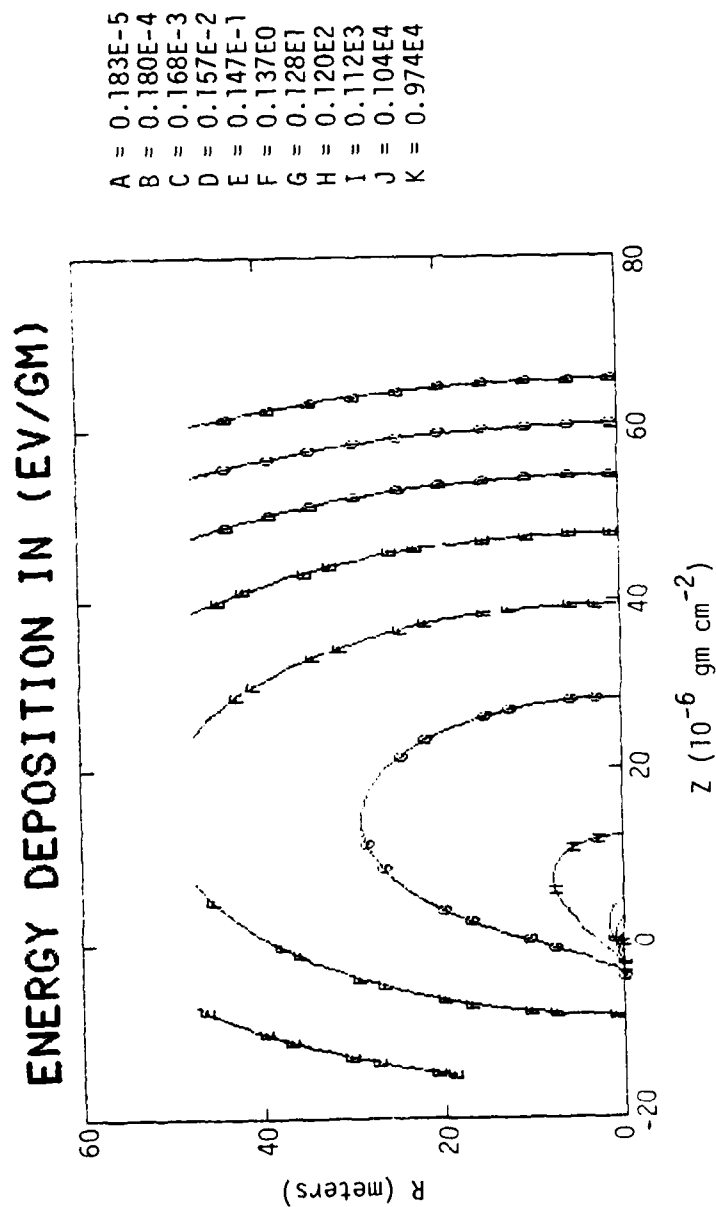


Figure 2-2. Volume deposition rate of 3-key electron beam in earth's magnetic field in normalized units for current of 1 electron/sec, $\theta_0 = 0^\circ$.

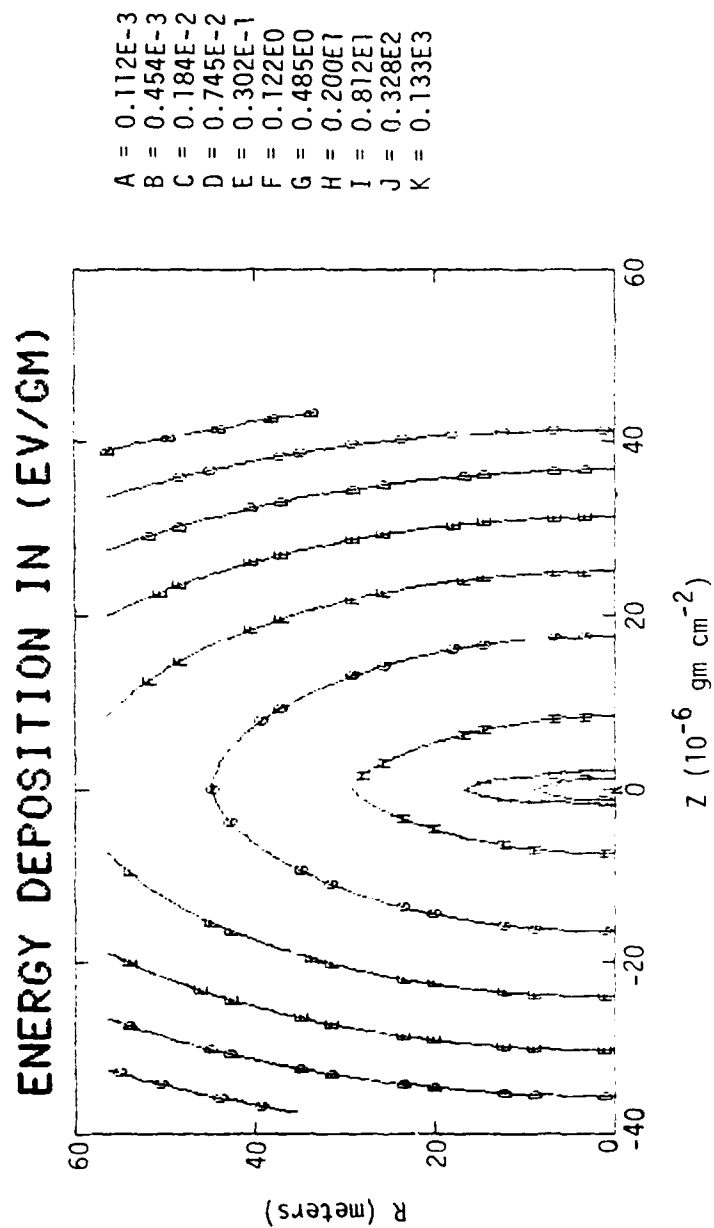


Figure 2-3. Volume deposition rate of 3-keV electron beam in earth's magnetic field in normalized units for current of 1 electron/sec, $\theta_0 = 88^\circ$.

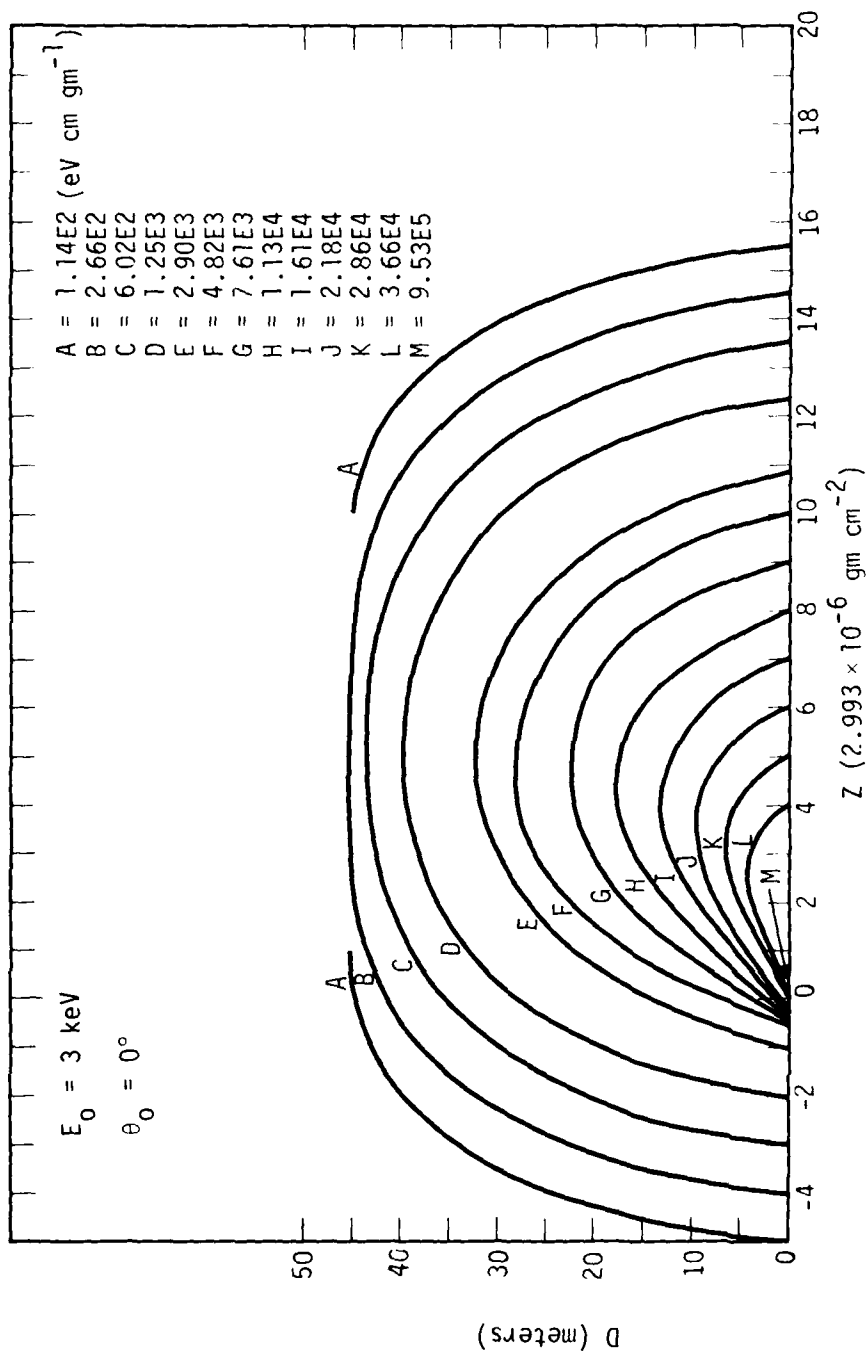


Figure 2-4. Contours of normalized brightness perpendicular to earth's magnetic field for a current of 1 electron/sec, $\theta_0 = 0^\circ$.

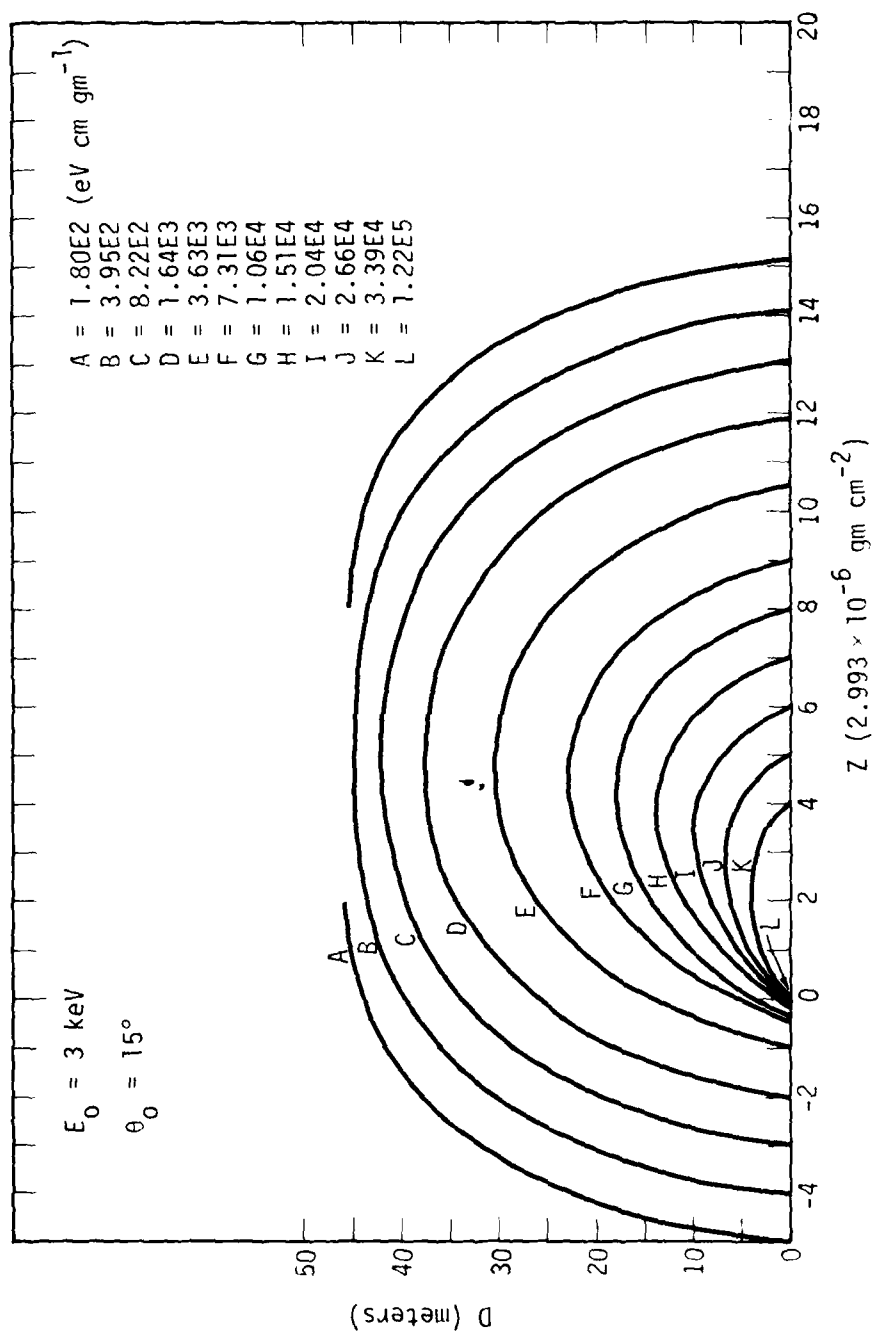


Figure 2-5. Contours of normalized brightness perpendicular to earth's magnetic field for a current of 1 electron/sec, $\theta_0 = 15^\circ$.

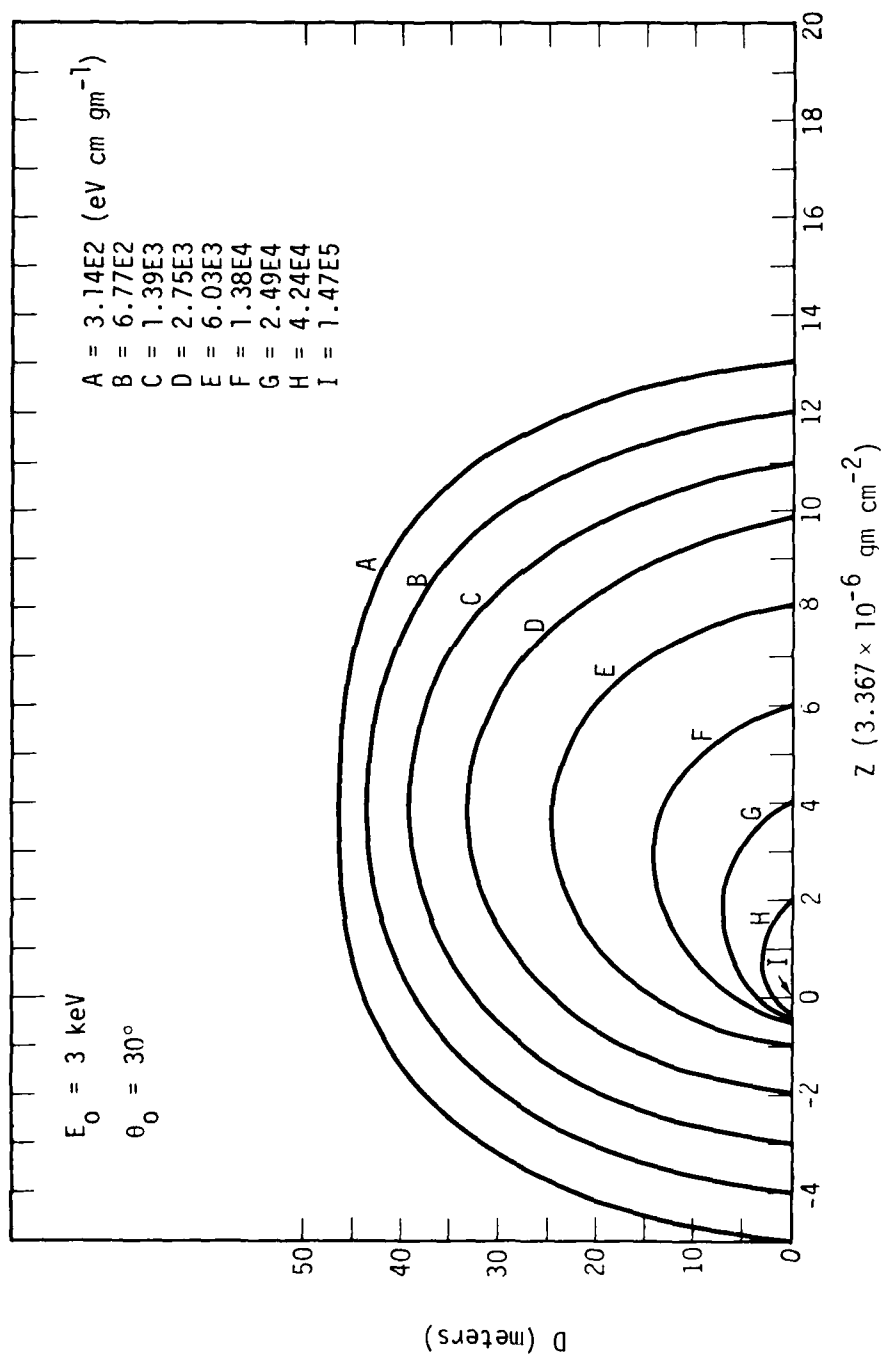


Figure 2-6. Contours of normalized brightness perpendicular to earth's magnetic field for a current of 1 electron/sec, $\theta_0 = 30^\circ$.

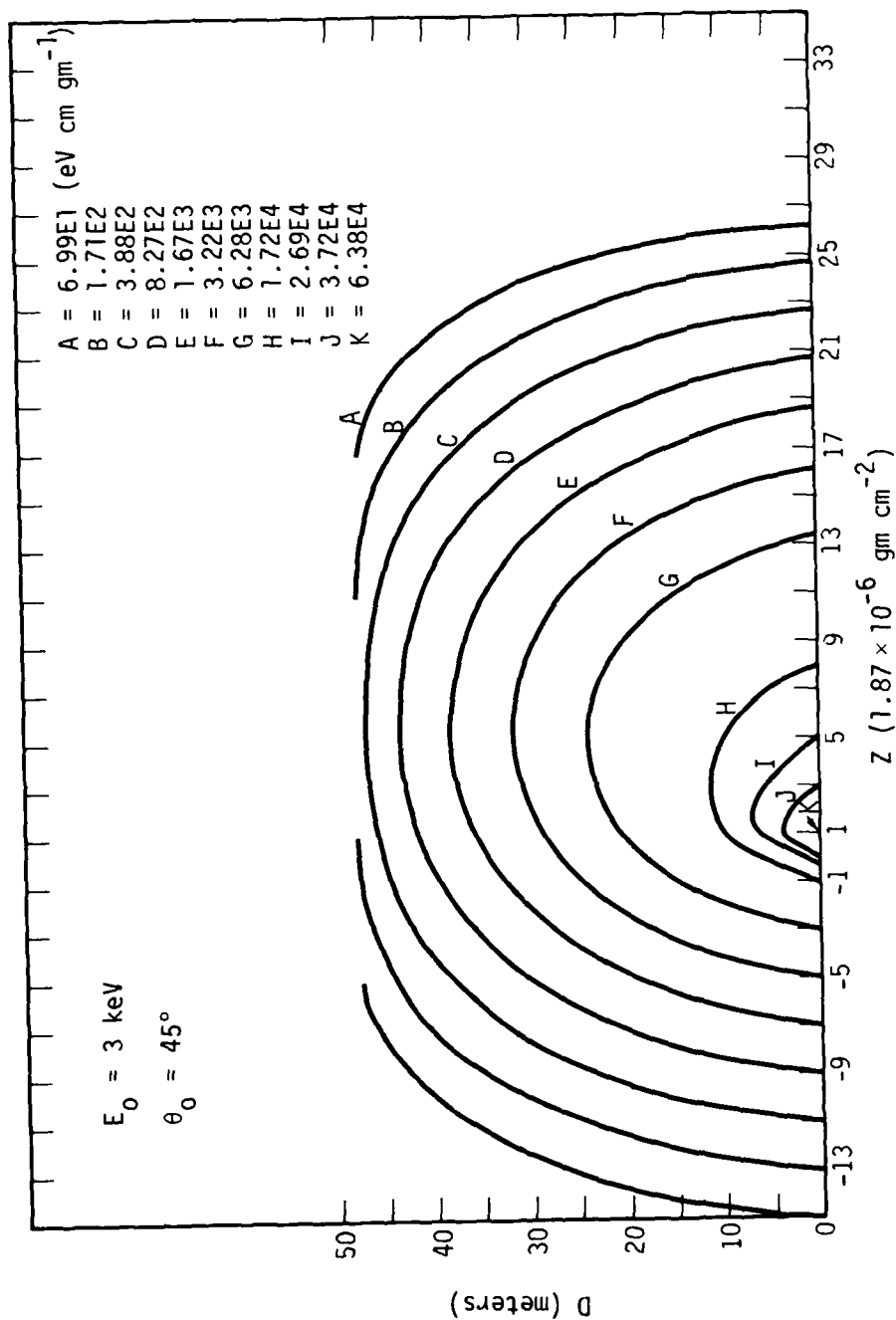


Figure 2-7. Contours of normalized brightness perpendicular to earth's magnetic field for a current of 1 electron/sec, $\theta_0 = 45^\circ$.

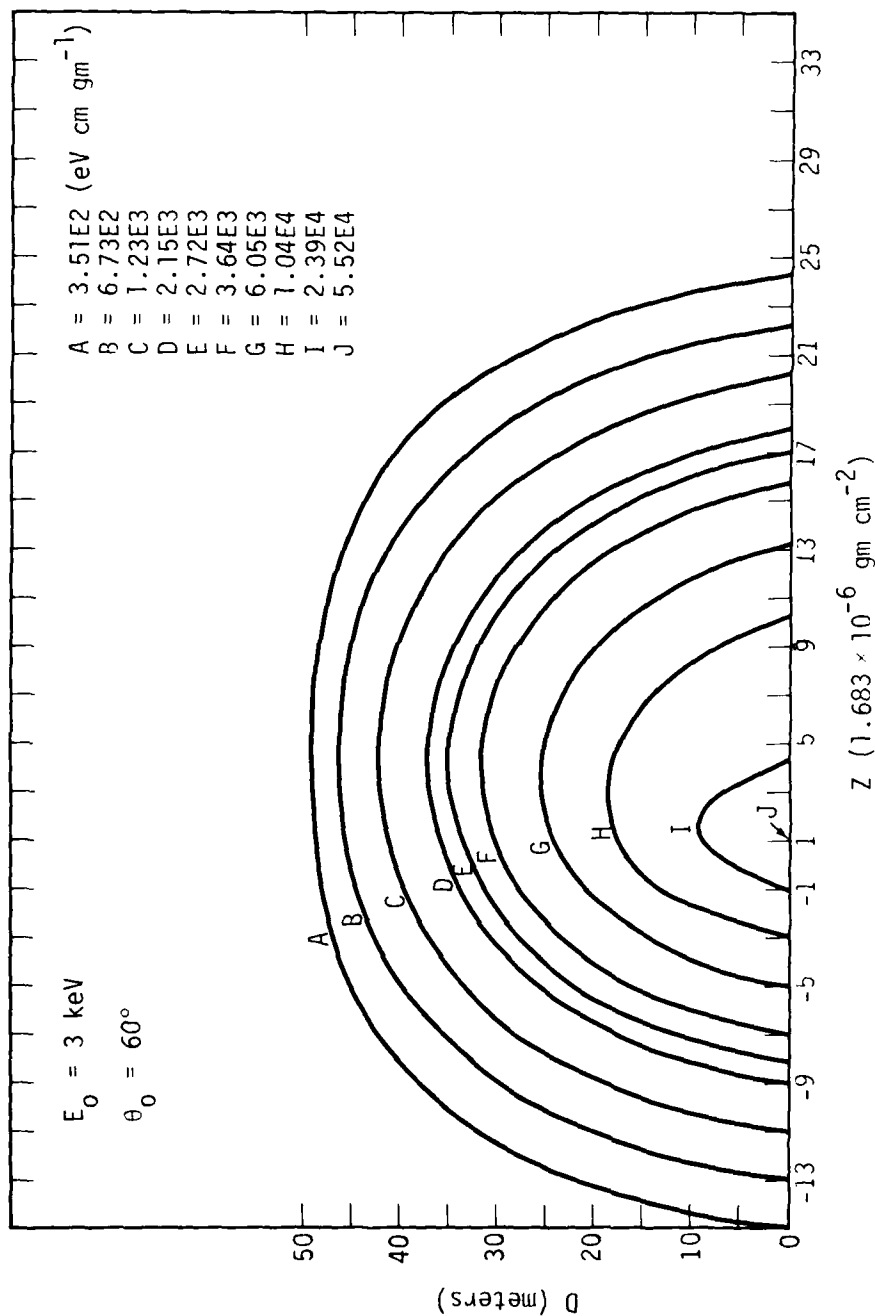


Figure 2-8. Contours of normalized brightness perpendicular to earth's magnetic field for a current of 1 electron/sec, $\theta_0 = 60^\circ$.

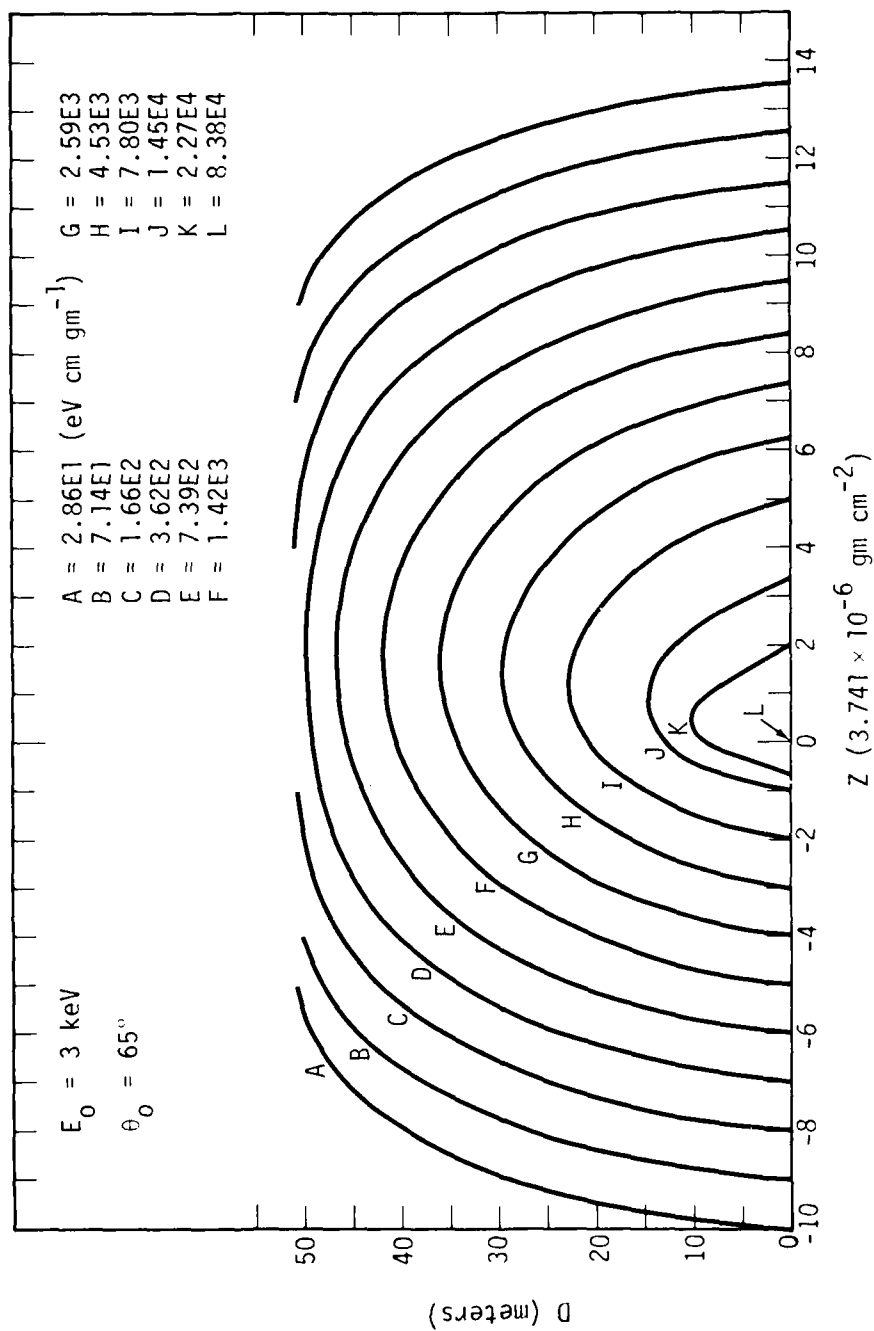


Figure 2-9. Contours of normalized brightness perpendicular to earth's magnetic field for a current of 1 electron/sec, $\theta_0 = 65^\circ$.

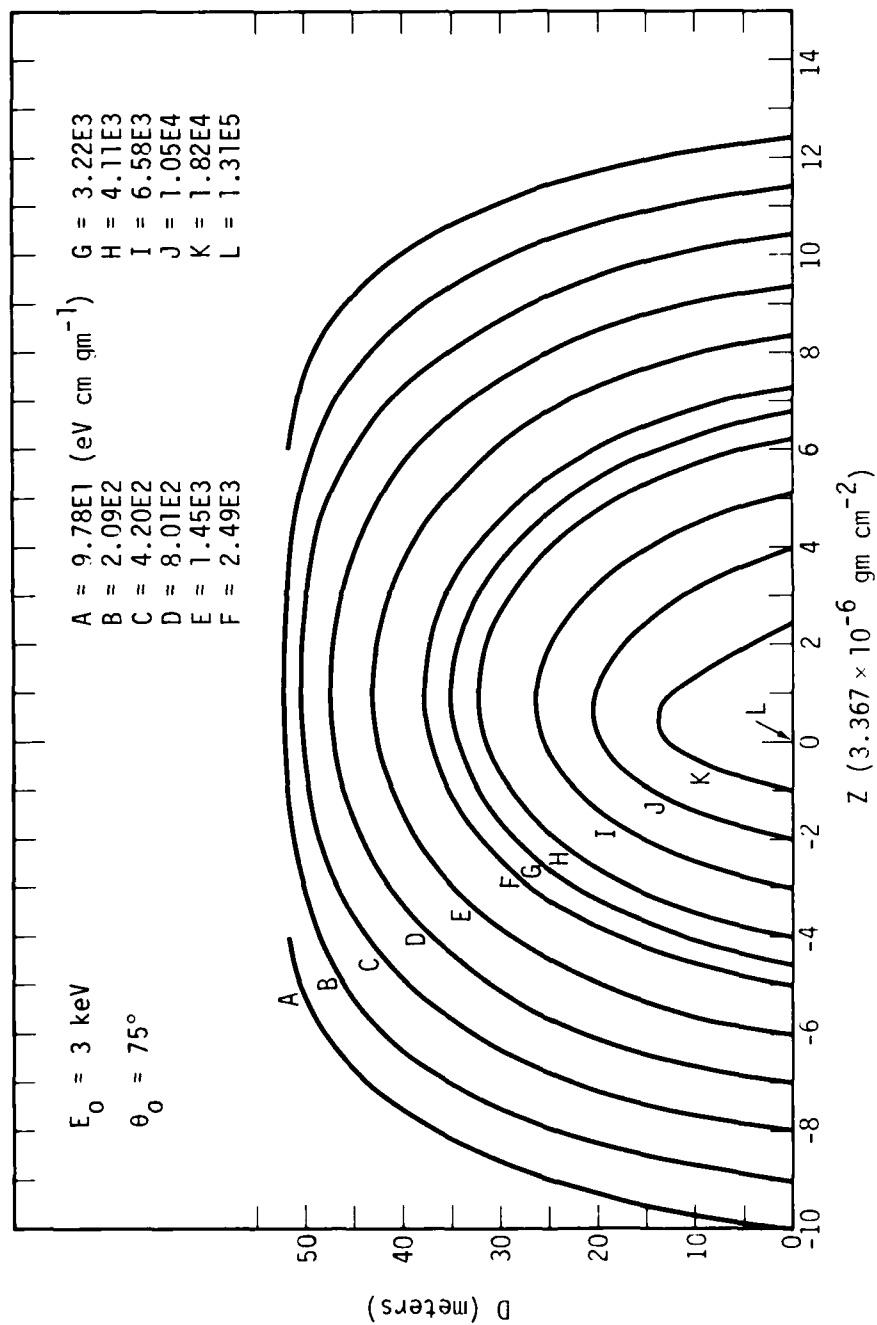


Figure 2-10. Contours of normalized brightness perpendicular to earth's magnetic field for a current of 1 electron/sec, $\theta_0 = 75^\circ$.

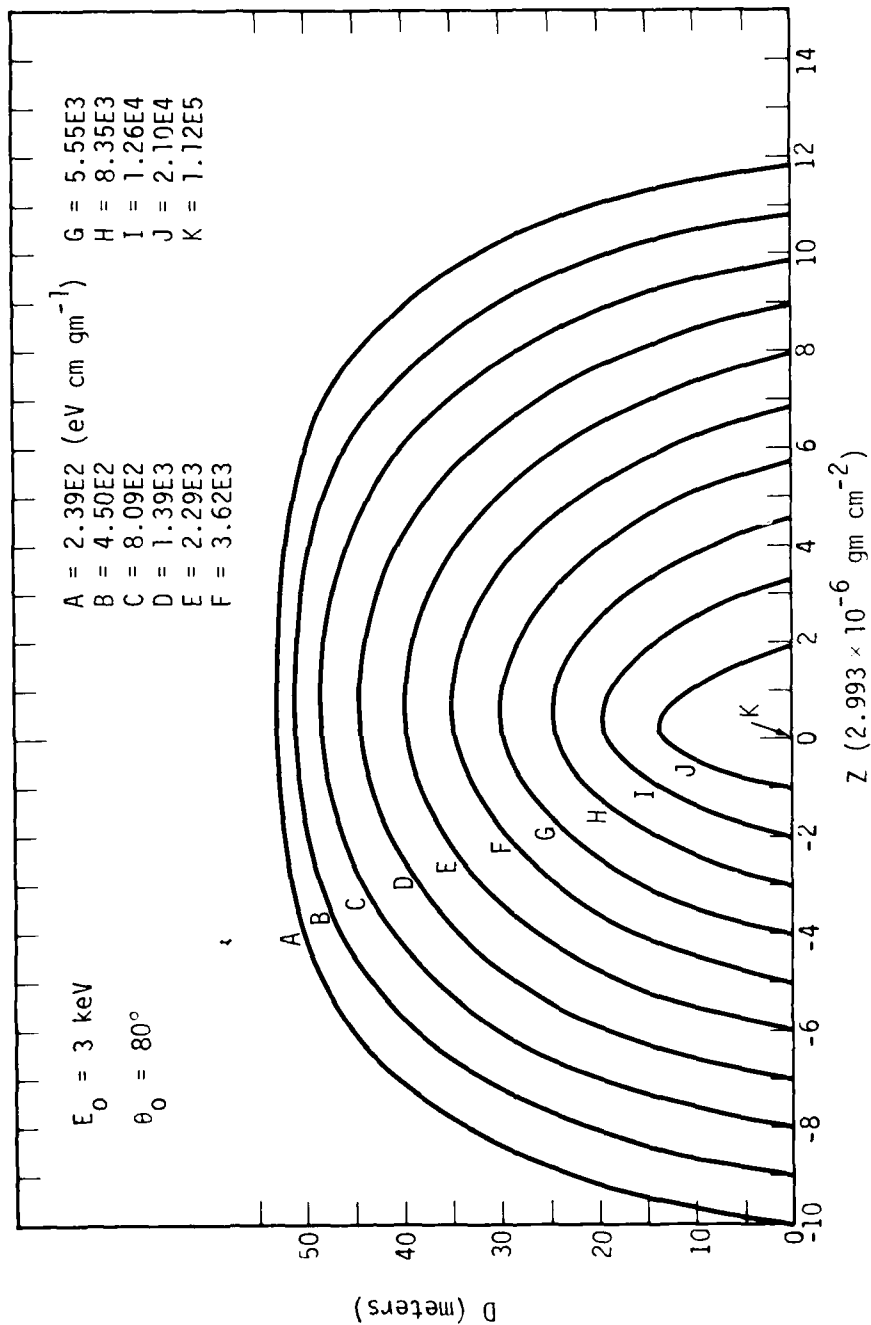


Figure 2-11. Contours of normalized brightness perpendicular to earth's magnetic field for a current of 1 electron/sec, $\theta_0 = 80^\circ$.

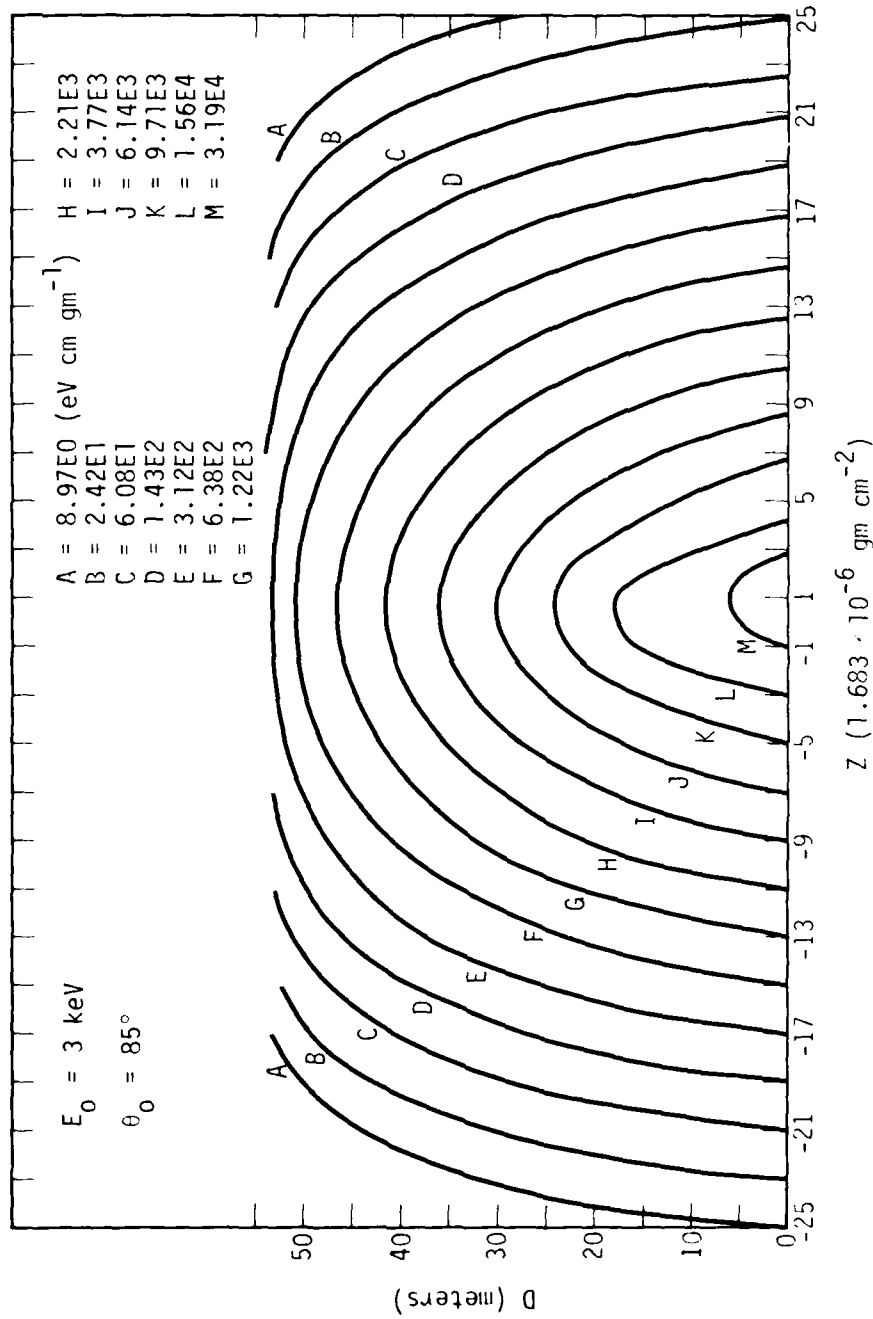


Figure 2-12. Contours of normalized brightness perpendicular to earth's magnetic field for a current of 1 electron/sec, $\theta_0 = 85^\circ$.

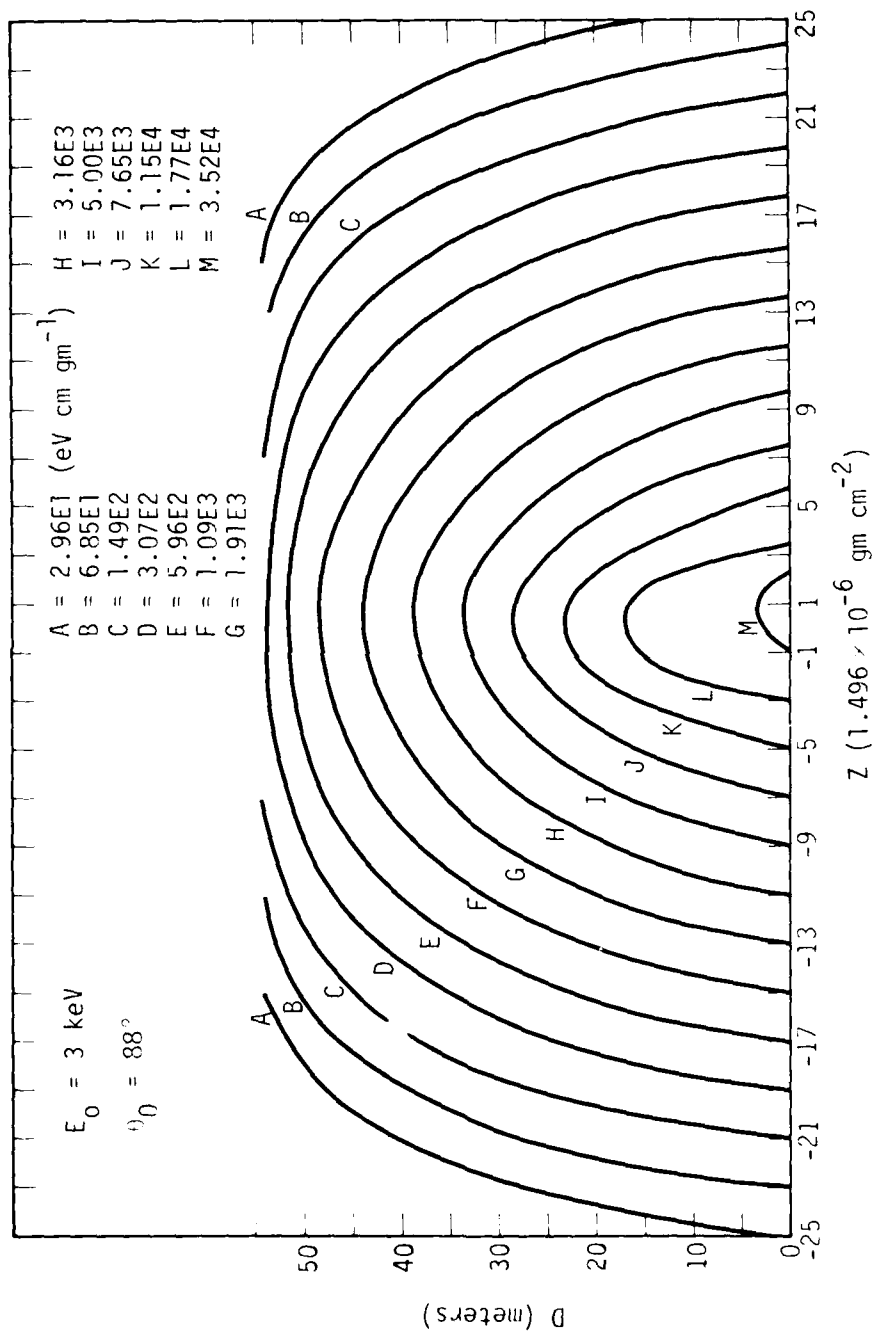


Figure 2-13. Contours of normalized brightness perpendicular to earth's magnetic field for a current of 1 electron/sec, $\theta_0 = 88^\circ$.

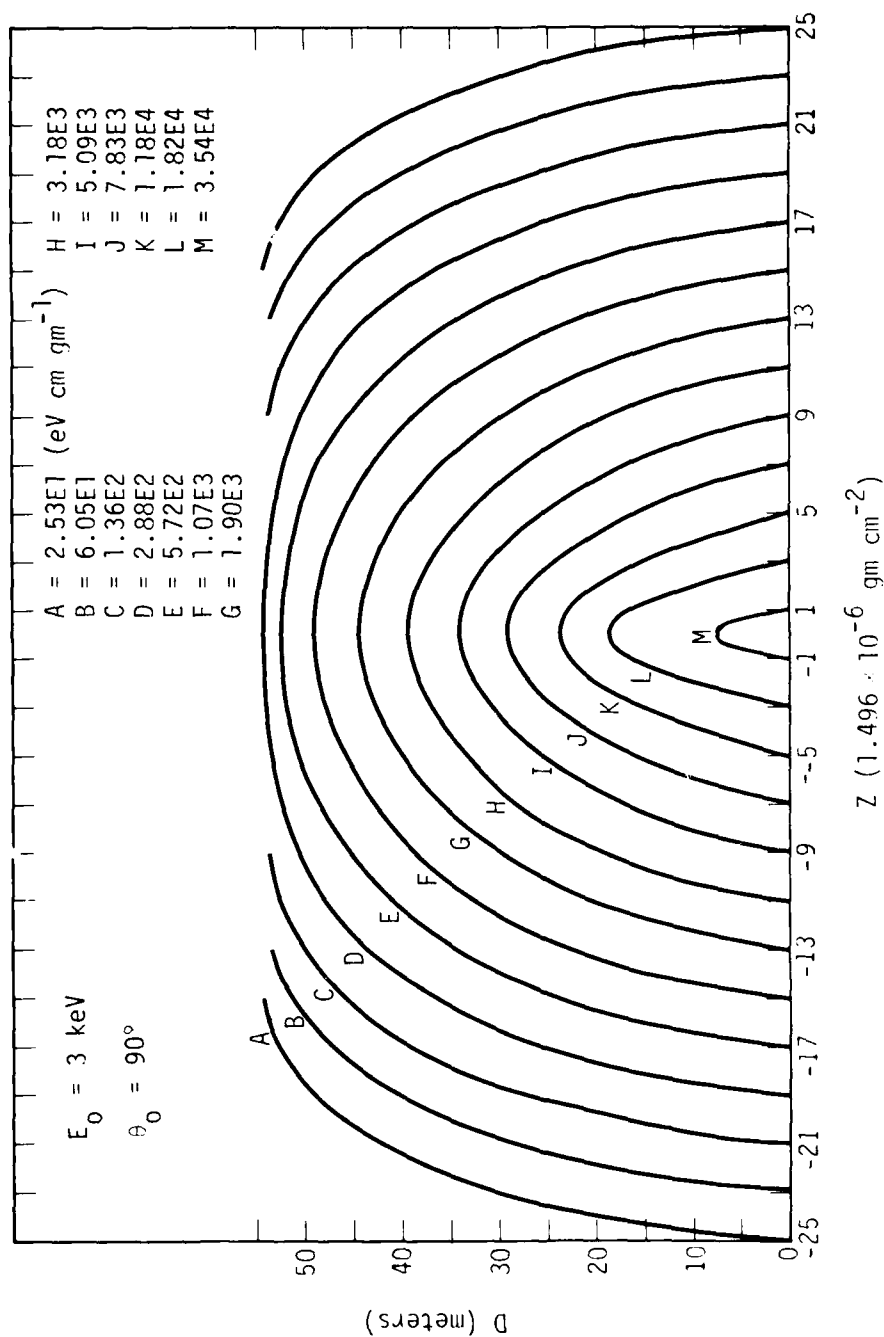


Figure 2-14. Contours of normalized brightness perpendicular to earth's magnetic field for a current of 1 electron/sec, $\theta_0 = 90^\circ$.

Figure 2-15 is a plot of the quantity $G(R)$, where

$$G(R) \equiv \int_{-\infty}^{\infty} \frac{d\varepsilon}{dt} (Z, R) dZ \quad (2-1)$$

is the column deposition rate, for a single electron, parallel to the magnetic field as a function of distance, R (meters), from the initial guiding field line. To convert to kilorayleighs (3914 Å), multiply the ordinate by 8.9×10^6 I (amps).

Figures 2-16 and 2-17 show the column deposition rate normal to (and through) the initial guiding field line as a function of distance, Z (gm cm⁻²), along the field. To convert to kilorayleighs (3914 Å), multiply the ordinate by 8.9×10^6 I(amps)ρ(gm cm⁻³).

COMPARISON WITH PRECEDE II IMAGE

To check the reasonableness of the foregoing brightness contours, we have attempted to compare our calculations with a video camera image recorded during the PRECEDE II experiment that took place over the White Sands Missile Range, New Mexico, on 13 December 1977. This experiment, described in Reference 2-2, was an engineering test of a rocket-borne electron accelerator module, providing a pulsed 3-kV, 7-A electron beam, and of a newly designed liquid-N₂ cooled infrared Michelson interferometer.

For orientation purposes, Figure 2-18 shows a plan view of the White Sands Missile Range including the rocket trajectory and various ground observation stations for the PRECEDE II event. The electron gun was operated in a pulse mode with a 6 sec period, 4.3 sec on and 1.7 sec off, on ascent between about 97 km and apogee at 102.34 km, and down to about 80 km on descent. The luminosity produced, including prompt air fluorescence and air afterglow emissions, was video recorded at the Stallion Optical Site (Figure 2-18) with the aid of the Air Force's 14-inch and 31-inch diameter

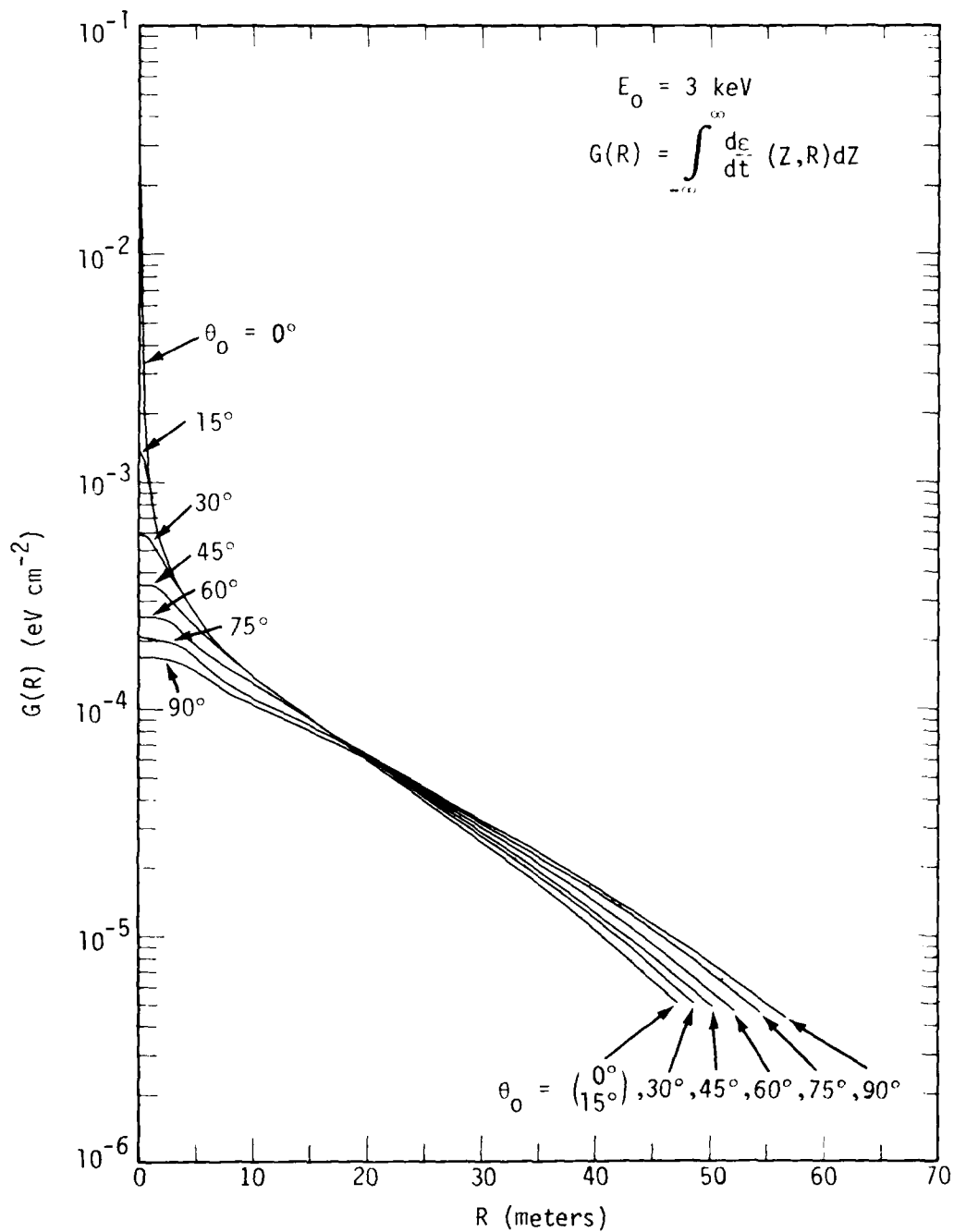


Figure 2-15. Column deposition rate, for a single electron, parallel to the earth's field, for parametric values of the electron's initial pitch angle.

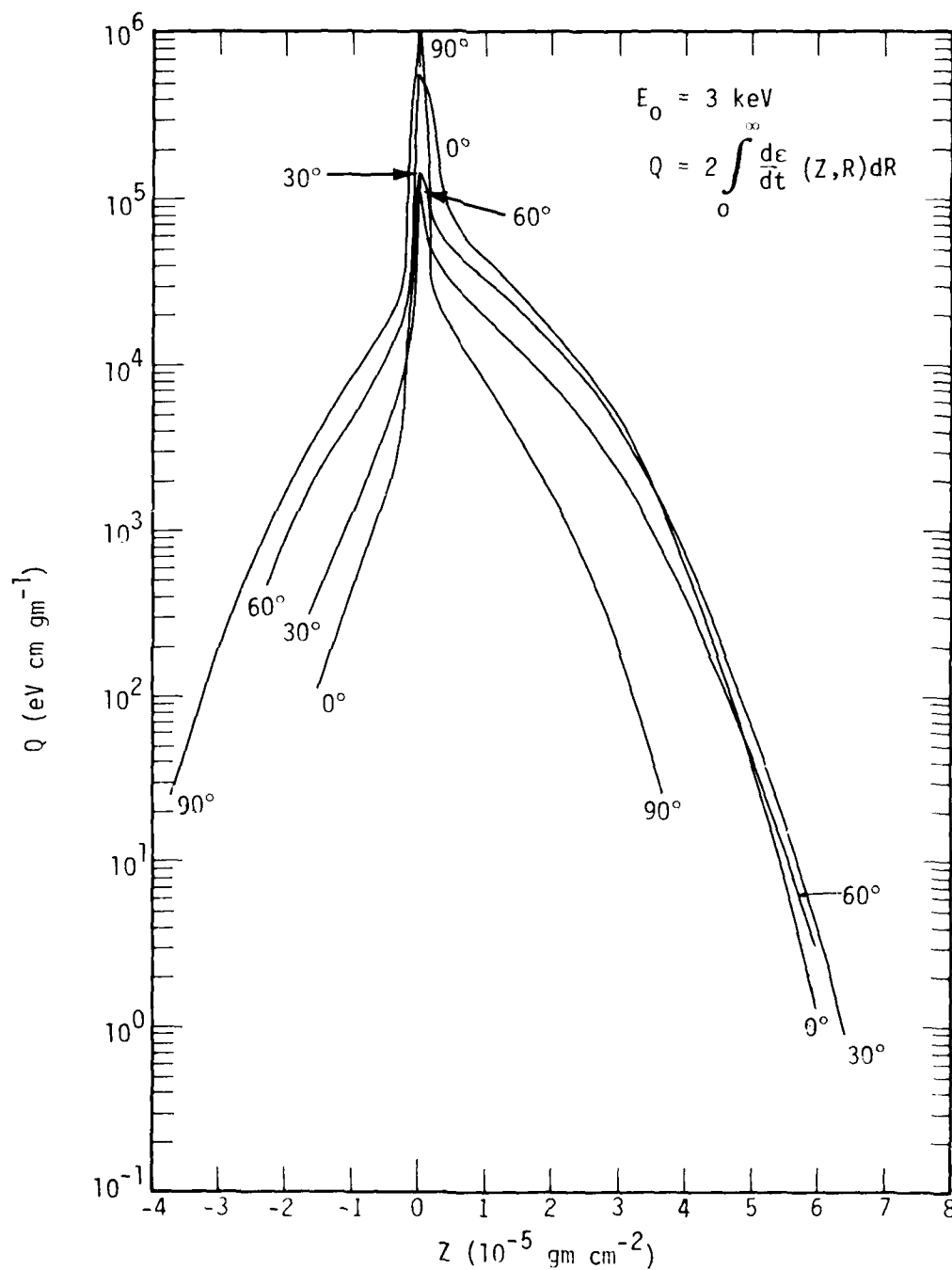


Figure 2-16. Column deposition rate, for a single electron, normal to the earth's field, for parametric values of the electron's initial pitch angle.

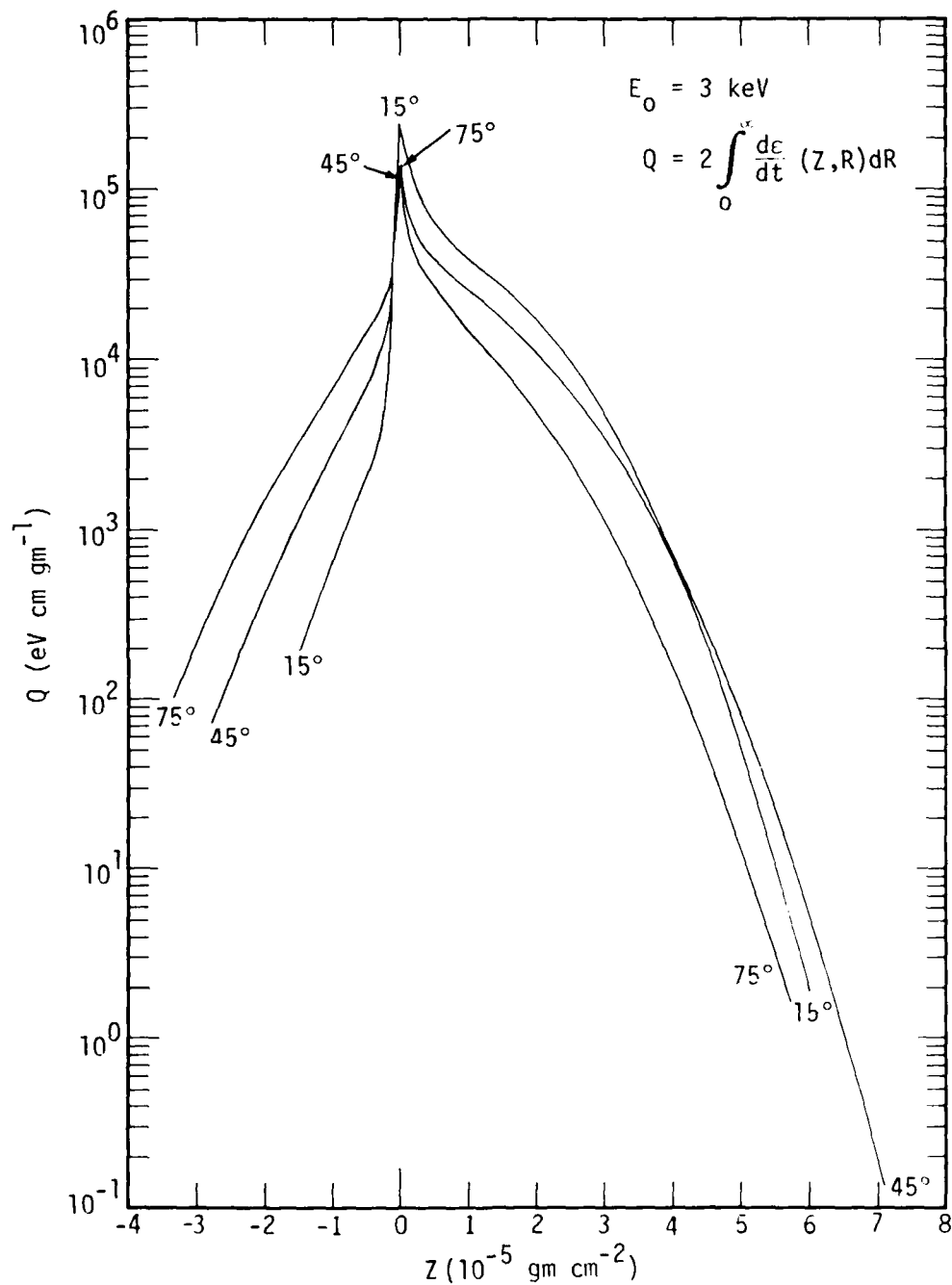


Figure 2-17. Column deposition rate, for a single electron, normal to the earth's field, for parametric values of the electron's initial pitch angle.

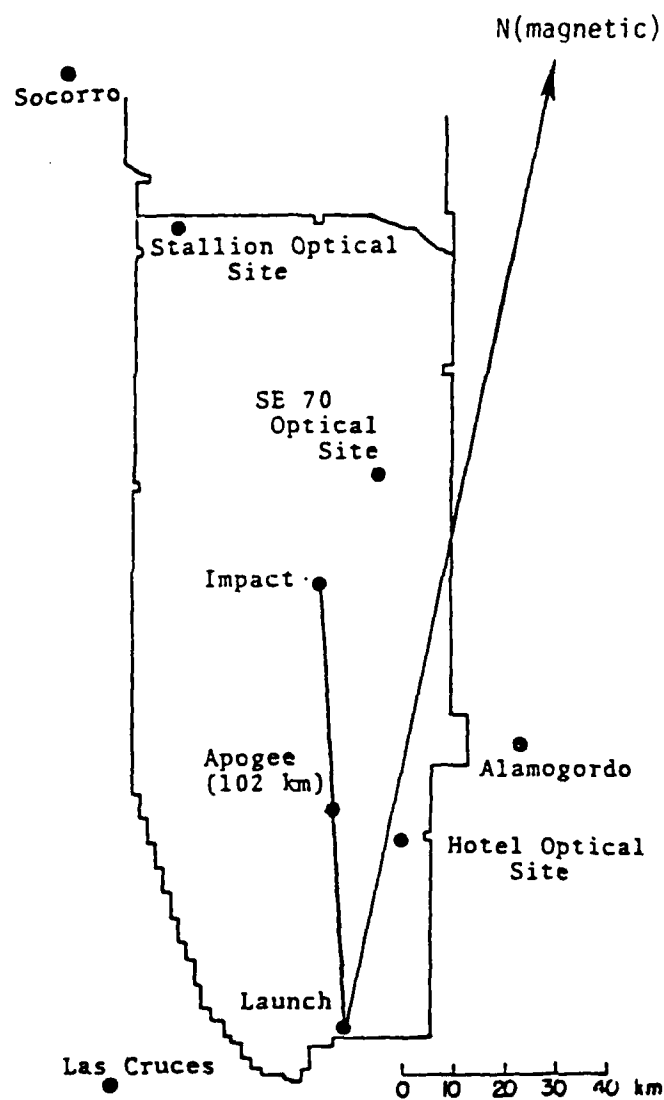


Figure 2-18. PRECEDE II experiment: White Sands missile range map (from Reference 2-2).

satellite tracking telescope systems (GEODSS facility). A pictorial sketch of the viewing geometry involved and the energy deposition volume aligned with earth's field, \vec{B} , is shown in Figure 2-19. A time sequence of video images (not shown in this report) for a single pulse period near rocket apogee shows first, at .04 sec after gun turn-on, a clean image due only to prompt fluorescence (Reference 2-3). By 0.6 sec the image is broader due to the appearance of afterglow emission. This afterglow emission tends to dominate and mask the prompt fluorescence-emitting deposition volume until gun shut-off at 4.3 sec.

The image that we have chosen to represent the luminous prompt deposition volume is the one recorded .04 sec after beam turn-on when the electron gun was just past apogee on descent at 102.3-km altitude. At this time, according to AFGL calculations (Reference 2-3), the gun was firing down the field (toward the earth) with the beam axis at a pitch angle of about 63° to the earth's field. However, the beam had a full cone angle of 30° and at .04 sec electrons with pitch angles from 48° to 80° are calculated to have been present. Based on the AFGL results, we estimate the mean pitch angle was about 65° .

Some calculated characteristics of the $3914\text{-}\overset{\circ}{\text{A}}$ emission intensity for a 7 amp, 3 keV electron beam at 102.3-km altitude are shown in Figures 2-20 and 2-21. Figure 2-20 shows the $3914\text{ }\overset{\circ}{\text{A}}$ brightness, normal to the magnetic field, as a function of distance* along the central (guiding) field line for electron pitch angles of 60° , 65° , and 80° . The peak brightness in these cases is 2.5, 1.8, and 2.4 MR, respectively. As seen, the intensity drops rapidly with distance in either direction along the field from the gun, falling by an order of magnitude 500 meters down the field.

* Distances measured upward along the field from the gun are positive; downward along the field are negative.

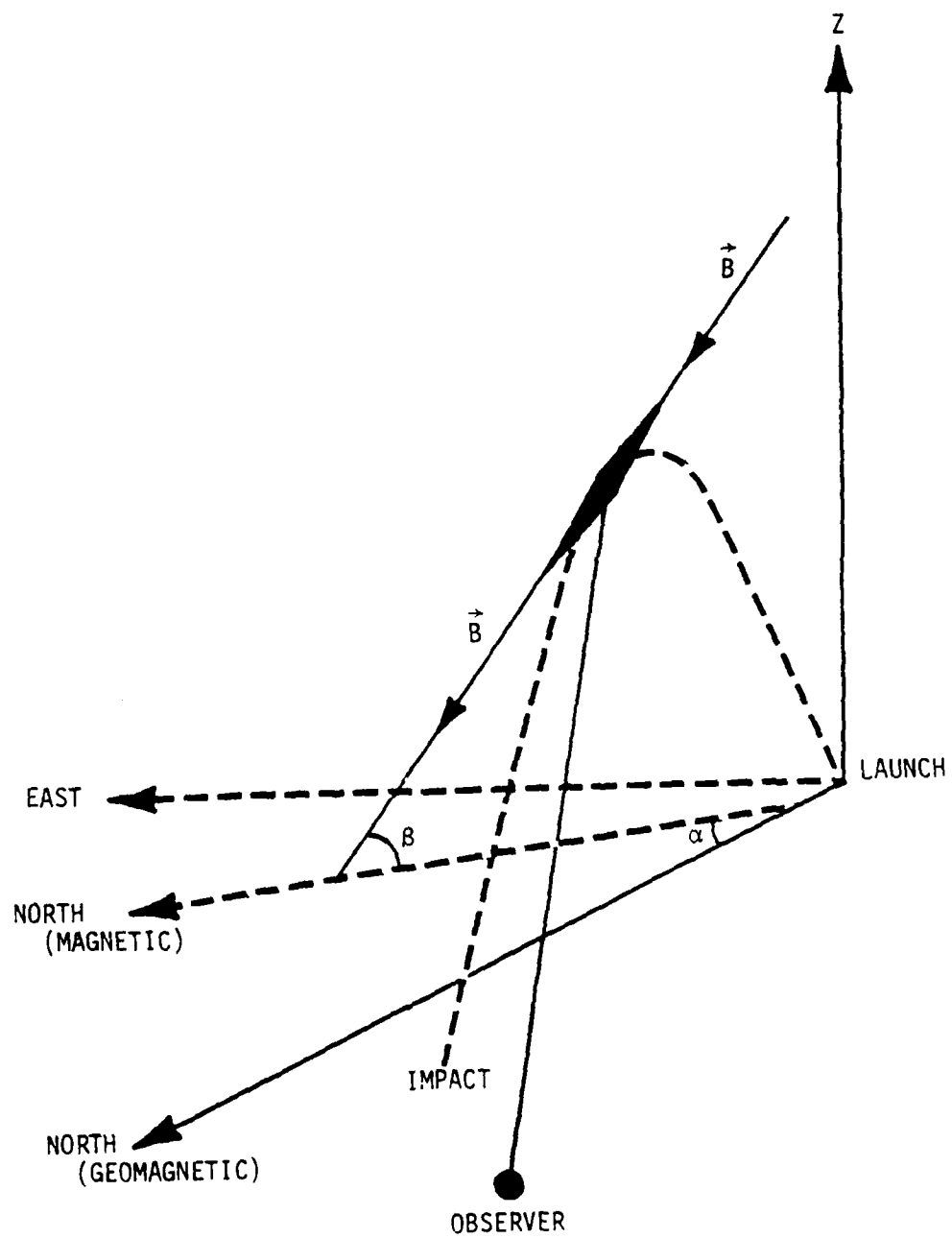


Figure 2-19. PRECEDE II geometry.

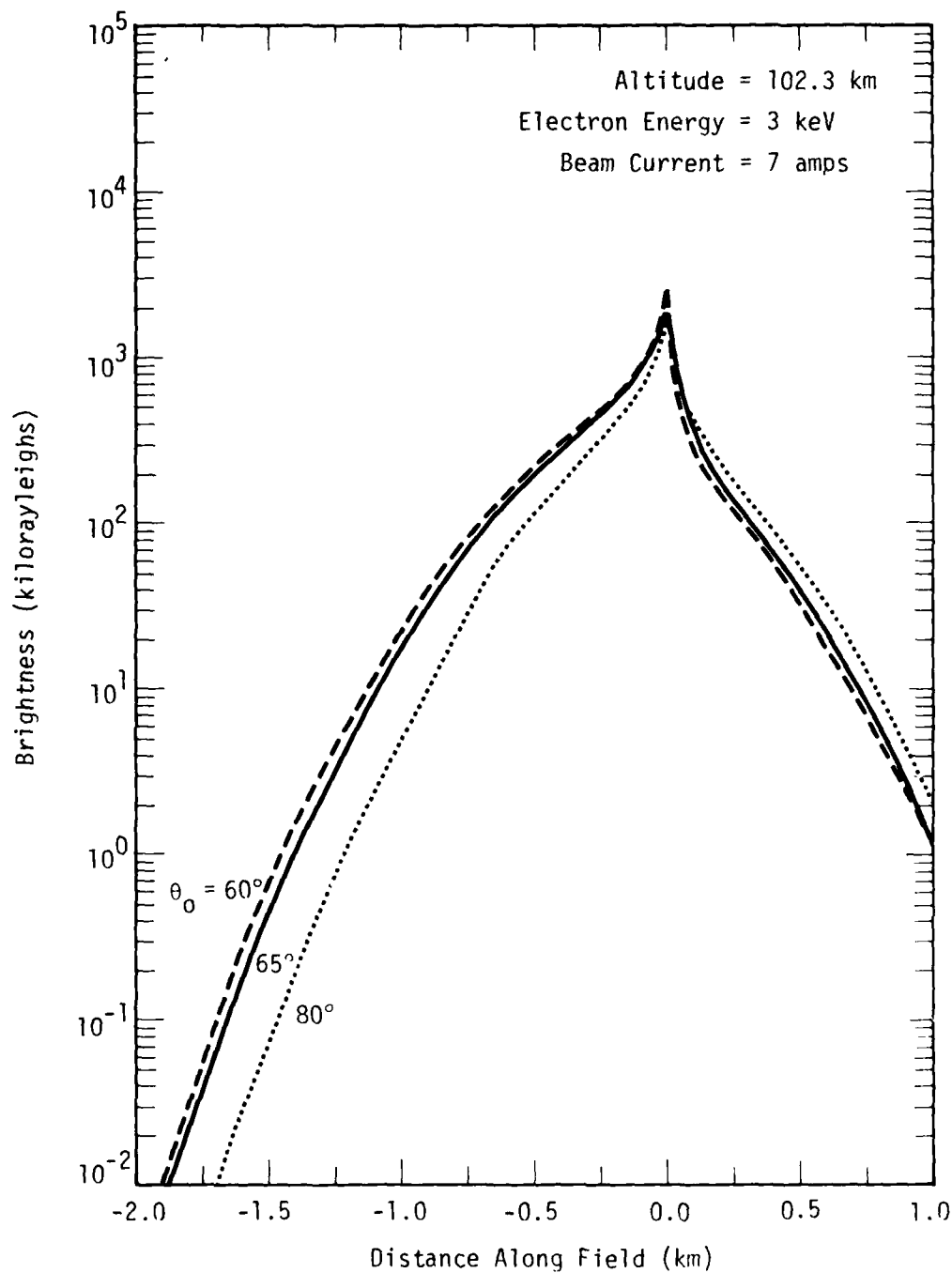


Figure 2-20. Calculated brightness at 3914 \AA normal to magnetic field as function of distance along central field line for three electron pitch angles.

Figure 2-21 shows the calculated off-axis brightness, at 3914 Å normal to the magnetic field, along a line through the electron gun, for pitch angles of 65° and 80°. The intensity is seen to drop rapidly in a direction away from the guiding field line, falling by an order of magnitude in a radial distance of about 20 meters.

To compare the observed image with our calculations, it has been necessary to correct it for the foreshortening effect, caused by the fact that the angle between the line of sight from the observer's station and the magnetic field was about 25° rather than 90° (see Figure 2-19), and to thus reconstruct the image as it would appear when viewed normal to the magnetic field. The middle profile in Figure 2-22 shows the results of our reconstruction. It has a maximum diameter, normal to the magnetic field, of about 70 meters, and down- and up-field dimensions of about 0.83 and 0.50 km, respectively. To compare the image with our calculated brightness contours, we have used Figures 2-4 to 2-14 to construct contours of constant brightness, in real space units for an altitude of 102.3 km, that have maximum radial diameters of 70 meters. Two of these contours are shown in Figure 2-22. The top one, calculated for a pitch angle of 80°, corresponds to a 3914-Å brightness of 78 kR. The bottom one, calculated for a pitch angle of 65°, corresponds to a brightness of 56 kR.

The most favorable comparison with the observed image in Figure 2-22 occurs for a pitch angle of 65°. Here the ratio of down-field to up-field lengths is about right. For smaller pitch angles, this ratio is too large, relative to the observed image; for larger pitch angles, it is too small. For example, for the 80° case shown in Figure 2-22, the down-field dimension is more nearly equal to the up-field dimension than what is actually observed.

It is gratifying that the most favorable comparison between theory and experiment occurs when the pitch angle for the calculated image corresponds to the mean pitch angle for the observed image. Better agreement

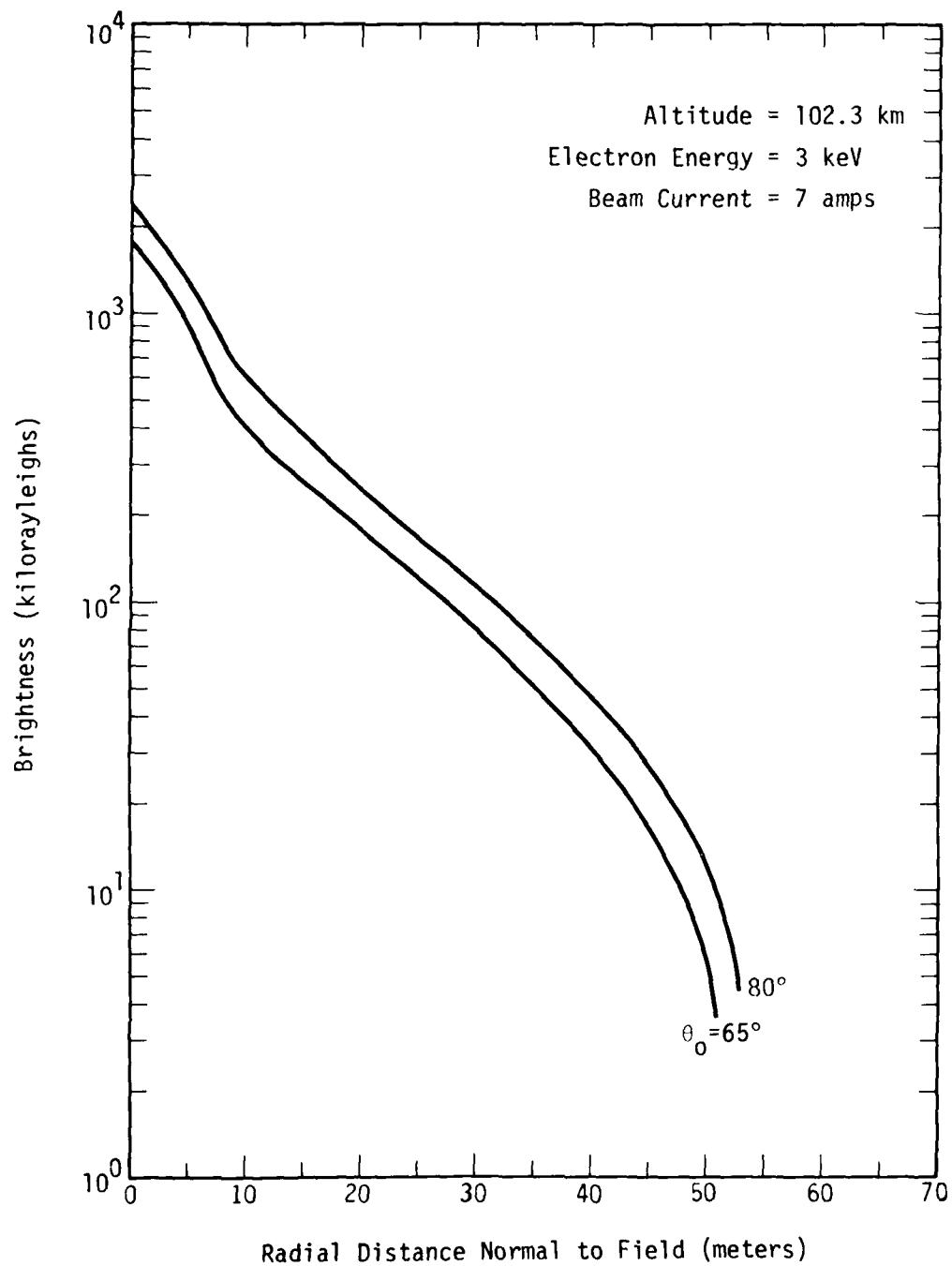


Figure 2-21. Calculated brightness at 3914 Å normal to magnetic field along line through electron gun.

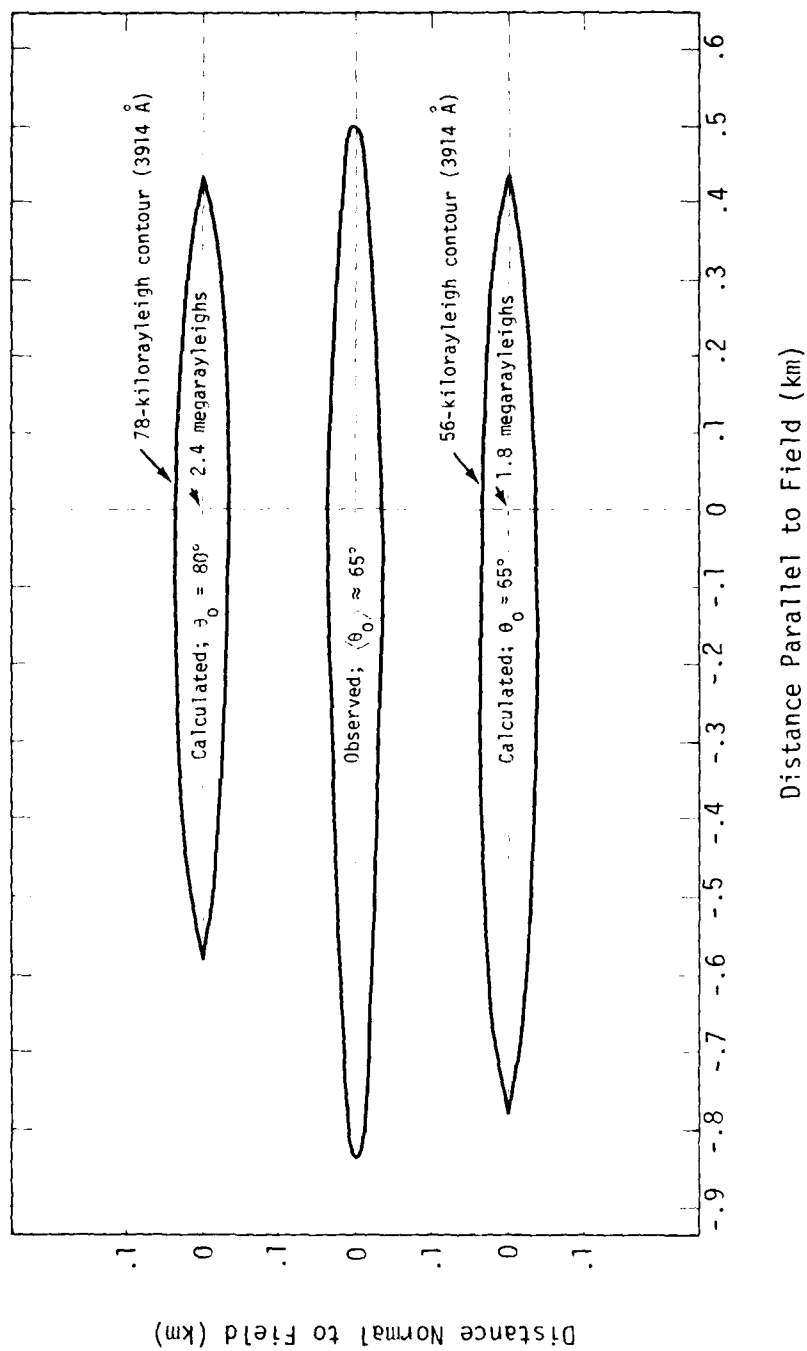


Figure 2-22. Projection of PRECEDE II image at 102.3-km altitude in magnetic meridian plane compared with calculated images for 65° and 80° pitch angles and radial diameter of 70 meters.

SECTION 3

EXCEDE:SPECTRAL CALCULATIONS

PRELIMINARY

The EXCEDE:SPECTRAL payload was launched from Poker Flat, Alaska on October 19, 1979 carrying 4 electron gun modules each capable of delivering an 8-A beam of 3 keV electrons. As described in Reference 3-1, the payload contained an array of ultraviolet, visible, and cryogenic infrared spectrometers, photometers, and both film and television cameras. In addition, a number of remote sites were used to augment the measurement capability of the experiment, with instruments that included ground-based film and television cameras.

One on-board camera, with fast black-and-white film and a filter cutting off above 4600 Å, measured principally emission in N_2^+ First Negative air-fluorescence bands and, secondarily, some N_2 Second Positive bands. It is reduced data from this camera that is of primary concern to us in this section. Some consideration will also be given to preliminary optical data from one of the ground-based cameras.

This experiment is the first of its nature to provide on board photographic data suitable for determining radiance contours of prompt emission, especially near 3914 Å. It is, therefore, particularly useful in checking the applicability of predictive codes that calculate the spatial dependence of the energy deposition rate surrounding electron beams in space. This section describes the results of a comparison between our code calculations and the reduced photographic data for one particular gun pulse, corresponding to an altitude of 123 km on rocket ascent.

Figure 3-1 (from Reference 3-1) shows the relative positions, on the rocket payload, of the four electron guns and the camera, along with a plan view of the projection of the camera's field of view and the region into which electrons from EXCEDE:SPECTRAL gun #4 may deposit energy. Positions of other instruments are indicated by the letters A through E. The guns were pulsed with on and off times nominally 4 and 2 sec, respectively, the electrons emerging from each gun in a cone of semi angle about 15° . On rocket ascent, the axes of the cones were approximately aligned with the earth's magnetic field with the guns firing up the field. For the pulse corresponding to an altitude of about 125 km on ascent, which we shall be considering here, only gun #4 was firing. The current was approximately 7 A.

CODE CALCULATIONS AND COMPARISONS WITH PHOTOMETRICS DATA

Our electron deposition code, described in Reference 2-1, was modified to calculate the energy deposition rate surrounding a 3-keV electron beam that emerges from the gun in a cone of half angle 15° , with axis aligned along the earth's field. The electrons are assumed to emerge uniformly over the initial pitch-angle range from 0° to 15° .

Figure 3-2 shows contours of constant energy deposition rate (eV gm^{-1}) for a single 3-keV electron with 0° pitch angle. The ordinate is the radial distance (m) from the central guiding field line, and the abscissa is the normalized distance (gm cm^{-2}) along the field line measured from the gun position. As described in Section 2, the contours can be converted to units of $\text{eV cm}^{-3} \text{ sec}^{-1}$ by multiplying by $6.25 \times 10^{18} \text{ I}_0$, and the distance along the field can be converted to units of cm by dividing by the local density, ρ .

Figure 3-3 shows corresponding contours for the case where the initial electron pitch angle is smeared over a cone, of half angle 15° , aligned with the magnetic field. Inspection of Figures 3-2 and 3-3 shows them to be very similar, except in the region near the electron gun where

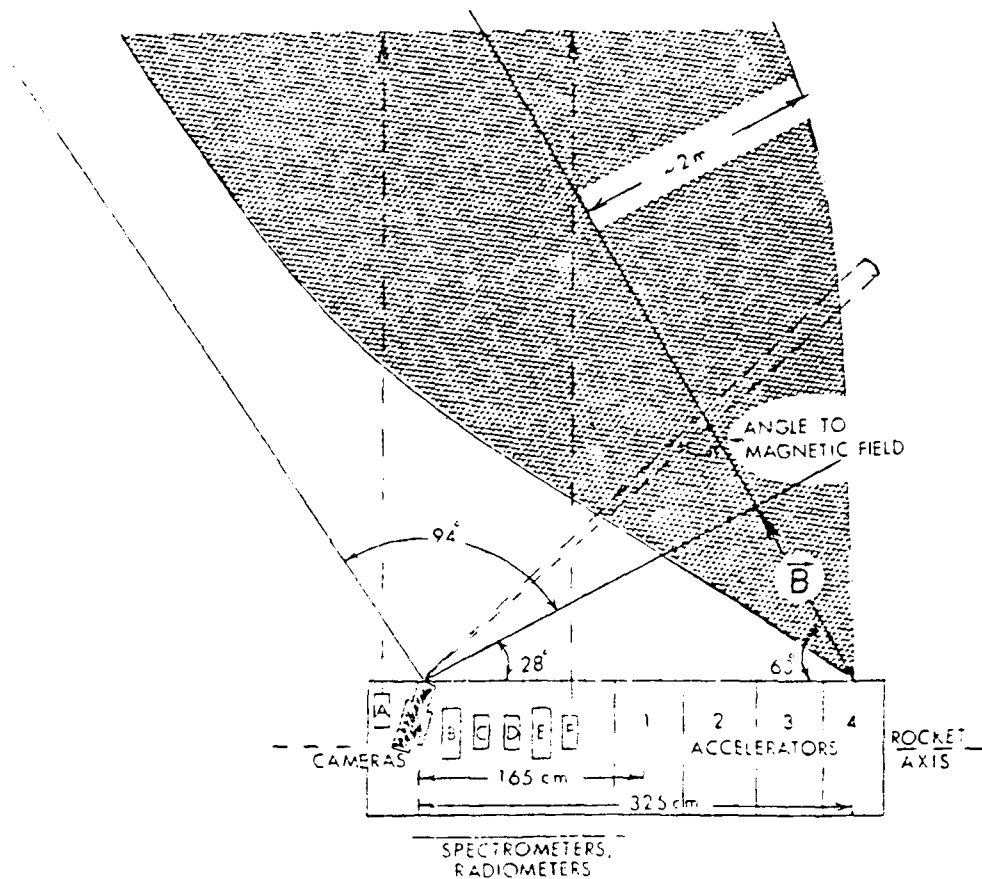


Figure 3-1. Plan view of the projection of the cameras' field of view and the region into which electrons from EXCEDE: SPECTRAL accelerator #4 deposit energy (as measured by the cameras) (from Reference 3-1).

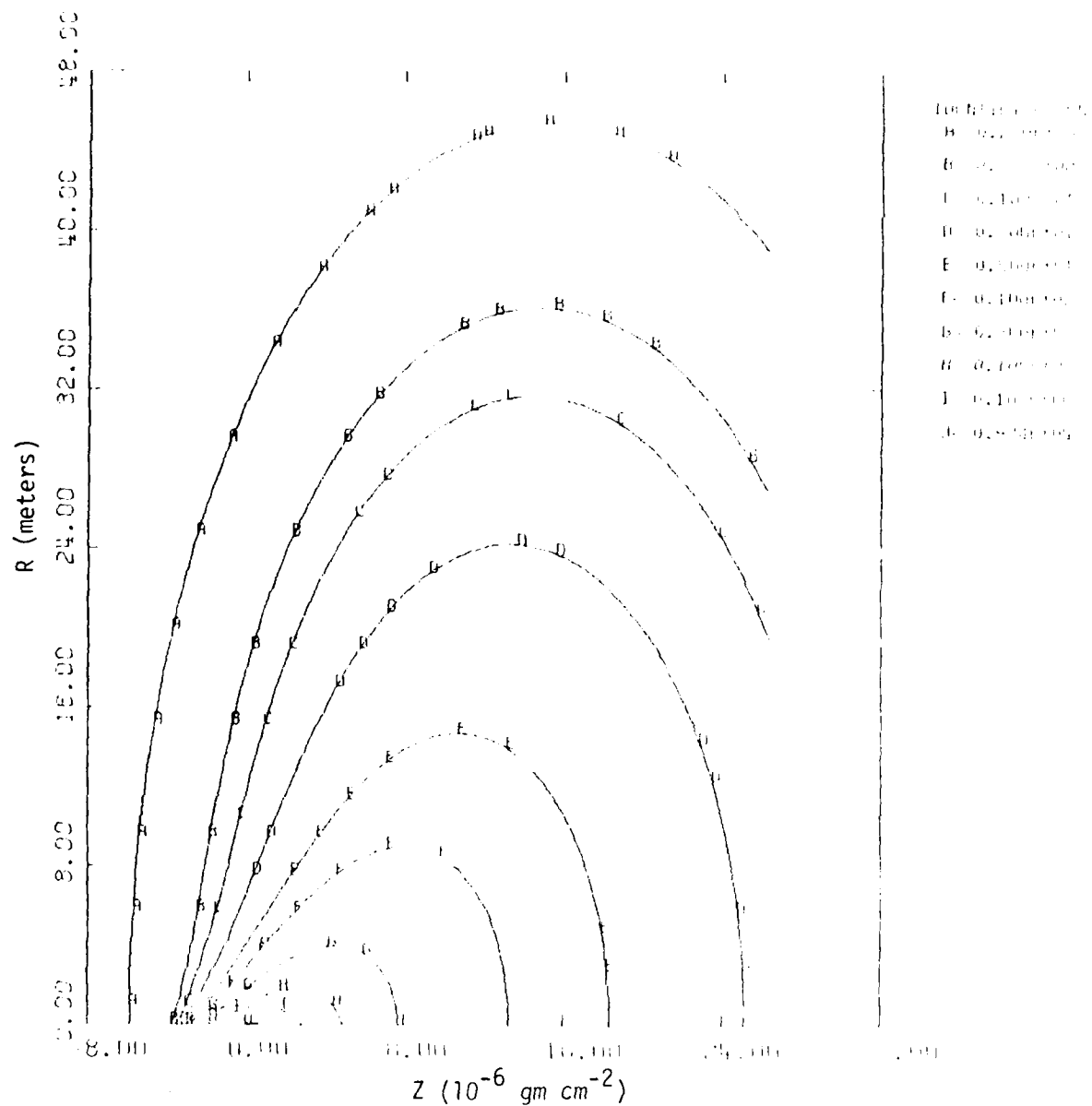


Figure 3-2. Volume deposition rate (eV gm^{-1}) of 3-keV electron beam in earth's magnetic field in normalized units for current of 1 electron/sec; beam initially parallel with 0° pitch angle.

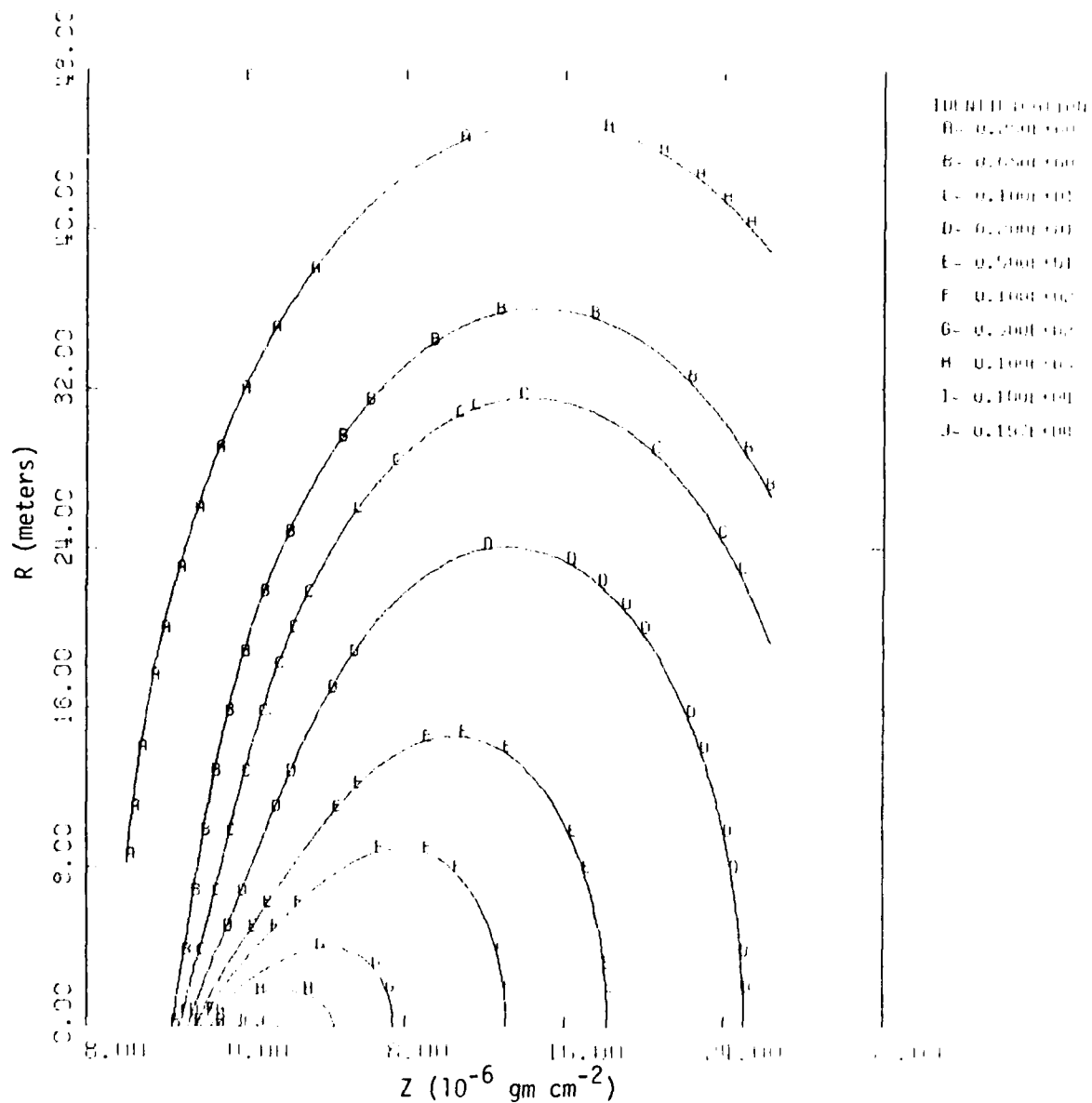


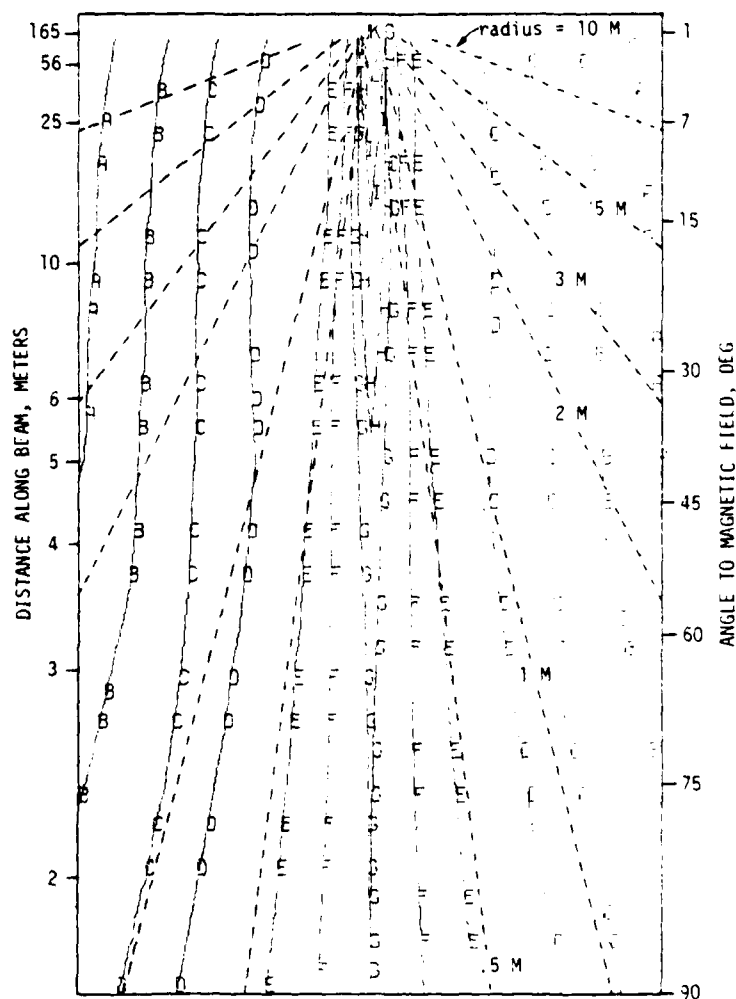
Figure 3-3. Volume deposition rate (eV gm⁻¹) of 3-keV electron beam in earth's magnetic field in normalized units for current of 1 electron/sec; beam initially in cone of semi angle 15° with axis parallel to magnetic field.

the "J" contour (actually just a point) is nearly 5 times larger in the 0° case than it is in the case of the cone where the energy is more smeared out. Furthermore, the peak value of the energy deposition (point "J") for the 0° case occurs at $z=0$ whereas, for the cone, it occurs at $z>0$.

Figure 3-4 (from Reference 3-1) shows the radiance distribution* in the image plane of the camera inferred by Photometries from densitometer analysis of the photographic film for a frame corresponding to an altitude of 123 km. Linear distances along the ordinate and abscissa of Figure 3-4 are proportional to distances on the film negative. Distance measured along the beam from the gun (#4) nozzle, and also the angle to the magnetic field (see Figure 3-1), are shown along the ordinate. Distance measured perpendicular to the beam for this projection is shown by dashed lines. The radiance contours are in units of $\text{ergs cm}^{-2} \text{ sec}^{-1} \text{ ster}^{-1}$. Notice the saddle point (relative minimum) in the intensity that occurs when the angle to the magnetic field is about 45° . The intensity is seen to increase from this point as the angle with the field decreases (viewing-region farther along the beam) and also as the angle increases (viewing-region closer to the gun).

Figure 3-5 is the calculated 3914 Å radiance in the image plane of the camera corresponding to the case of a parallel beam with 0° initial pitch angle. Figure 3-6 is the corresponding representation for a conical beam of half angle 15° , and is the appropriate one to compare with the photographic data shown in Figure 3-4. These results are based on an assumed fluorescence efficiency at 3914 Å of 4.5×10^{-5} , an atmospheric density of $1.717 \times 10^{-11} \text{ gm cm}^{-3}$, and a beam current of 7 A.

* These radiance values are for the entire filter band that extends from about 3600 Å to 4700 Å. They are assumed to equal approximately 1.5 times the radiance values due to 3914 Å emission alone (Reference 3-2). The actual data, referred to here as the "in-band data," when reduced by a factor of 1.5, will be referred to as the "3914 Å data."



IDENTIFICATION (ergs $\text{cm}^{-2} \text{sec}^{-1} \text{ster}^{-1}$)

A = $0.600\text{E}-02$ E = $0.500\text{E}-01$ I = $0.100\text{E}-01$

B = $0.750\text{E}-01$ F = $0.100\text{E}-00$ J = $0.100\text{E}-01$

C = $0.100\text{E}-01$ G = $0.240\text{E}-00$ K = $0.10\text{E}-01$

D = $0.150\text{E}-01$ H = $0.400\text{E}-01$

Figure 3-5. Calculated radiance (3914Å) distribution in image plane of camera (corresponding to Figure 3-4) if electron beam were initially parallel with 0° pitch angle.

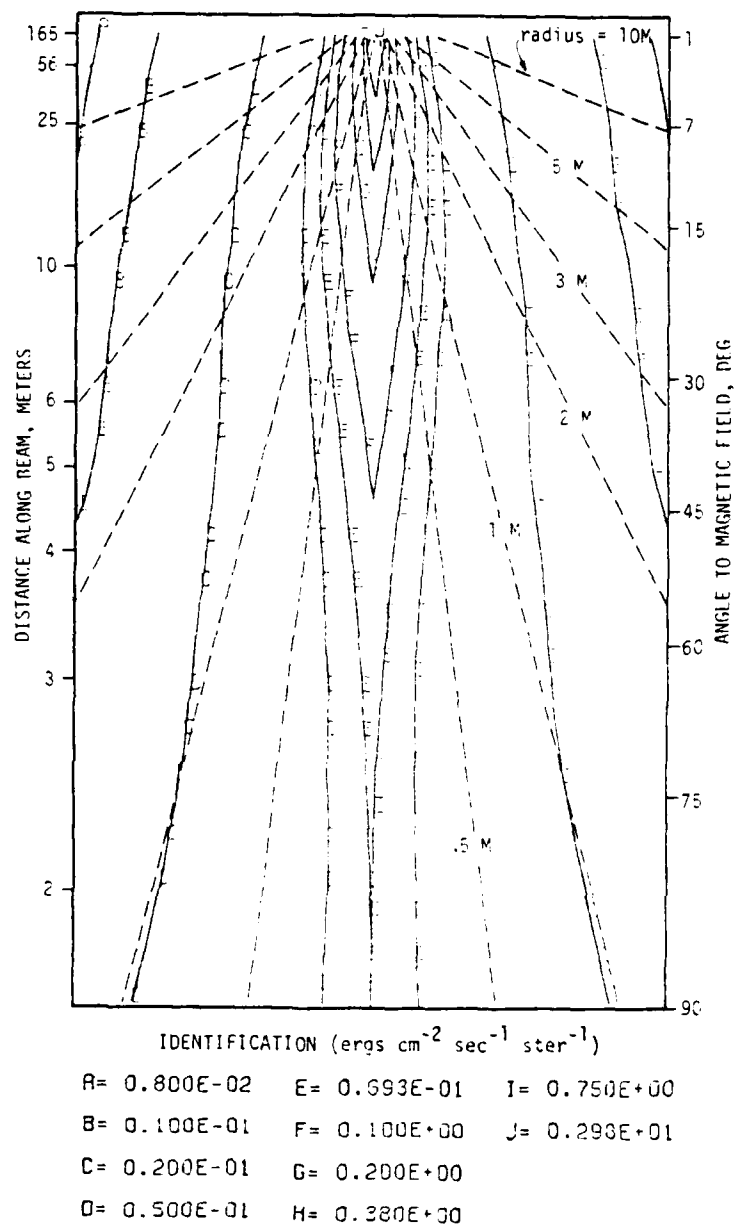


Figure 3-6. Calculated radiance (3914Å) distribution in image plane of camera (corresponding to Figure 3-4) for the case where the electron beam is initially in a cone of semi angle 15° with cone axis parallel to the earth's field.

Comparison of Figures 3-4 and 3-6 reveals a large discrepancy in both the magnitude and shape of the contours of constant brightness, especially in the region within about 7 meters of the electron gun. The saddle point, or relative minimum on axis at about 4.5 meters from the gun, that is evident in the data of Figure 3-4, is entirely missing in Figure 3-5. Rather, the calculations show a monotonic decrease in brightness as the viewing angle to the magnetic field increases from 1° to 90° . When the sight path is normal to the magnetic field (on-axis viewing point = 1.625 meters from gun #4), the observed in-band intensity (Figure 3-4) is about $15 \text{ ergs cm}^{-2} \text{ sec}^{-1} \text{ ster}^{-1}$ (or $10 \text{ ergs cm}^{-2} \text{ sec}^{-1} \text{ ster}^{-1}$ at 3914 \AA). The calculated intensity (Figure 3-6), under the same viewing conditions, is about $0.07 \text{ ergs cm}^{-2} \text{ sec}^{-1} \text{ ster}^{-1}$, which is 142 times smaller than the 3914 \AA data.

At larger distances from the gun, the discrepancy between the data and the calculations is less but still significant. For example, the difference between the calculated and observed projected radiance (at 3914 \AA) for points at 6, 10, and 25 meters from the gun are factors of about 4, 6, and 10, respectively, whereas the brightest point calculated (corresponding to a viewing angle to the magnetic field of 1° , or to a point 165 m from the gun) is a factor of only 1.6 less than the brightest down-the-field point shown in the data.

The apparent radial dimension of the beam, inferred from the data, is also larger than that inferred from the calculations. For example, at a point 25 m from the gun, Figure 3-4 shows that the 0.1 "in-band" brightness contour is at a radial distance of about 4.5 m. This is to be compared with a corresponding radial distance of only about 2 m inferred from Figure 3-6.

Further comparisons between the photographic data and the calculations are shown in Figures 3-7 and 3-8. Figure 3-7 shows the brightness

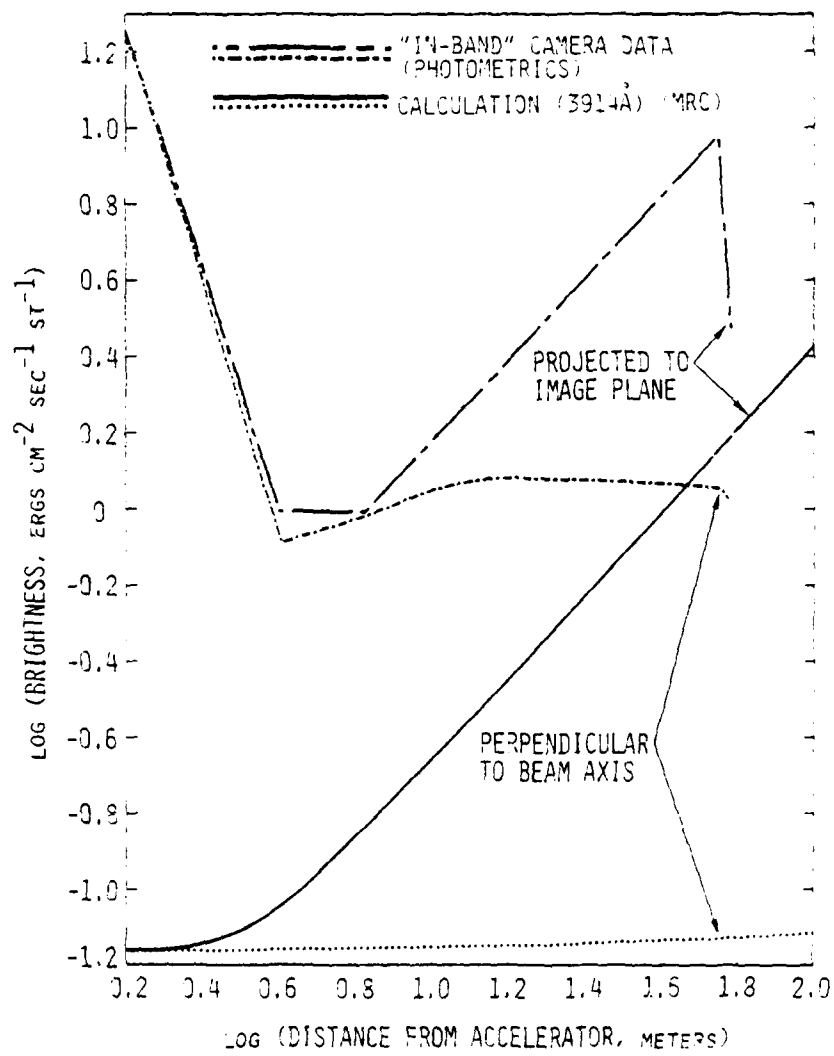


Figure 3-7. EXCEDE:SPECTRAL radiance projected to the onboard camera along the electron beam axis and also viewing perpendicular to the axis; calculation and photographic data compared.

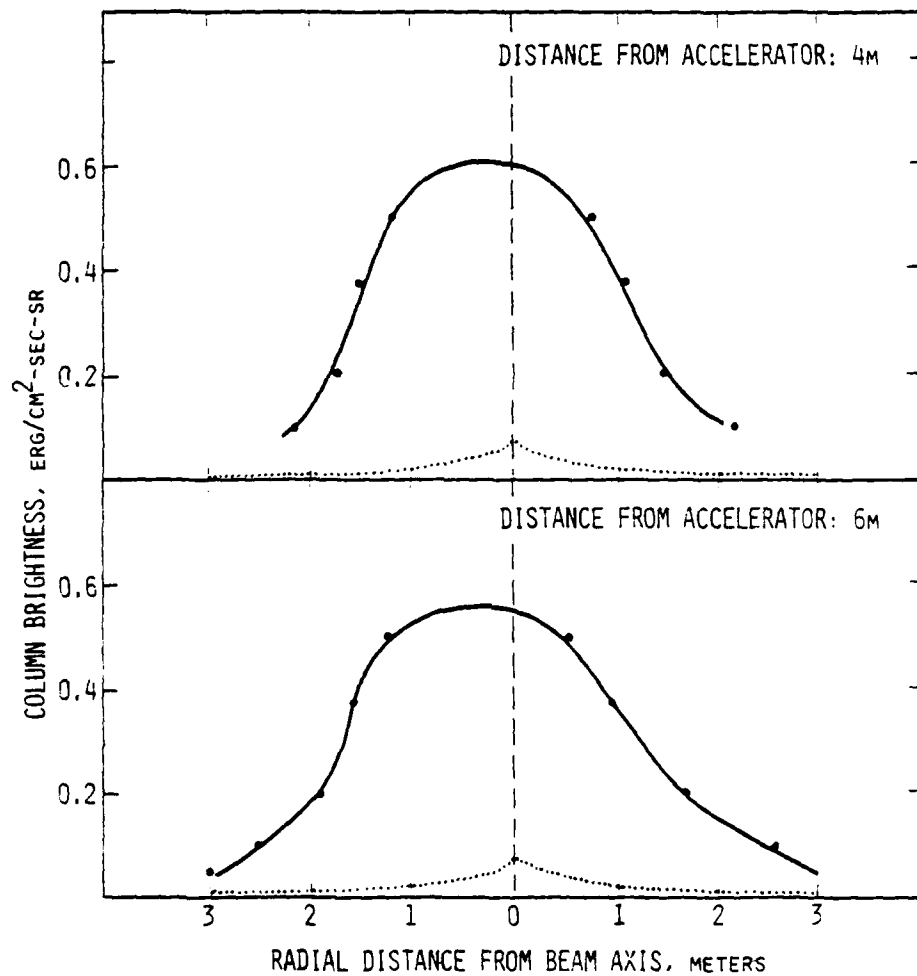


Figure 3-8. Radiance projected to the onboard camera transverse to the electron beam's axis. Solid curves are "in-band" data from Ref. 3-1; dotted curves are calculated values for 3914Å.

projected to the image plane, and also normal to the beam axis, as functions of distance from the accelerator. Both the "in-band" photographic data (from Reference 3-1) and the calculated 3914 \AA values are shown. To directly compare these curves, the calculated brightness should be multiplied by 1.5. Consistent with Figure 3-4, the photographic data show a rapid decrease in intensity in the first 4 meters from the accelerator. However, beyond about 9 or 10 meters from the accelerator, the observed intensity normal to the beam remains roughly constant at a value of about $1.15 \text{ ergs cm}^{-2} \text{ sec}^{-1} \text{ ster}^{-1}$. In this region the behavior of the data and the theoretical curves are quite similar, except in magnitude, with the calculated intensity normal to the beam being about a factor of 10 less than the 3914 \AA data.

Figure 3-8 shows the observed and calculated radiance projected to the onboard camera transverse to the electron beam's axis at distances of 4 m and 6 m from the accelerator. Again, for a direct comparison of these curves, the calculated values should be multiplied by a factor of 1.5. When this is done, we find that the calculated brightness through the beam axis is less than the photographic data by factors of about 8.5 and 8.0 at 4 m and 6 m, respectively, from the gun.

COMPARISON WITH PRELIMINARY TIC DATA

Ground-based photographic observations of the EXCEDE:SPECTRAL event were made by the Technology International Corporation (TIC). Some preliminary results of their densitometric analysis for three pulse images have been made available to us (Reference 3-7). These preliminary results give relative radiance values as a function of distance along the beam.

We have attempted to compare our calculated values of radiance normal to the beam with the TIC data for the case of a pulse recorded when the payload was at an altitude of 124 km on ascent. The results are shown

in Figure 3-9. The photographic data have been arbitrarily normalized to the calculated intensity at a distance of 3 km along the beam from the accelerator. The origin in the abscissa scale is the position of the electron gun.

Although the peak relative intensity is not given for the photographic data, it is reasonable to conclude from Figure 3-9 that the ground-based data support a considerable enhancement of the brightness in the vicinity of the gun, at least qualitatively consistent with the on-board camera observations. Firmer conclusions can be reached only after absolute radiance values have been assigned to the TIC data.

COMMENTS

It is obvious from the foregoing comparisons that the theoretically-inferred deposition of energy surrounding the electron beam does not agree with the photographic data, at least in the region within a few meters of the electron gun where the observed intensity is up to two orders-of-magnitude greater. There is, thus, a very bright region near the gun that the theory, based on single particle deposition in an ambient atmosphere, does not predict. As for the beam farther from the gun, it is difficult to unravel accurately its behavior by analysis of the onboard photographic data (Figure 3-4) because most lines of sight from the camera transverse the close-in bright region which tends to mask emission from the more remote regions. Thus, it seems to us that the field data presented in Figure 3-7, for distances greater than about 10 meters from the accelerator, may overestimate the actual radiance normal to the beam axis. However, even if this is the case, it is unlikely that the distortion could account for the full factor of 10 difference between theory and experiment.

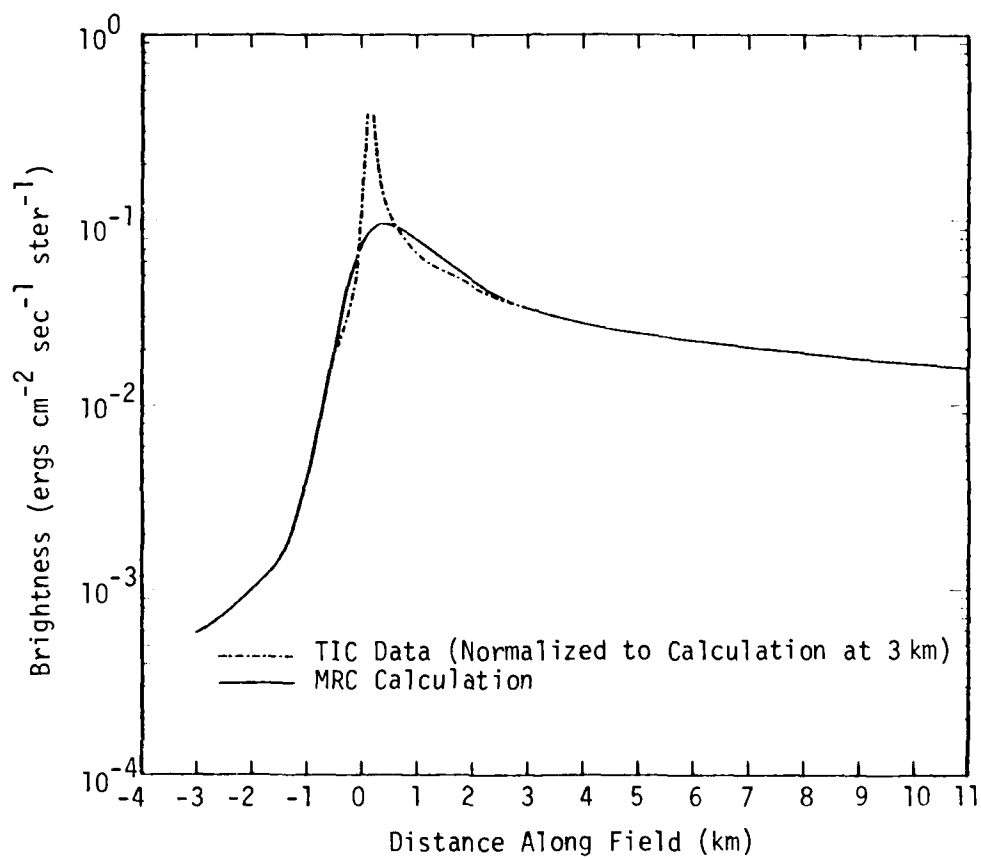


Figure 3-9. EXCEDE:SPECTRAL radiance (3914Å) normal to beam axis at 124 km (ascent); calculation and photographic data compared.

The theory, upon which our code is based, and which is described in detail in Reference 2-1, gives results that are in good agreement with laboratory data by Grün (Reference 3-3) and Cohn and Caledonia (Reference 3-4), and with other codes, for example the Lockheed code (Reference 3-5). Therefore, to the extent that the electron beam can be treated as a collection of independent particles depositing energy in the ambient atmosphere, we feel that our code results are essentially correct. On the other hand, the photographic data reduction is probably also essentially correct.

The reason for the discrepancy is not known for sure at the present time. However, it may well owe its origin to the possibility that the beam electrons near the gun are not acting independently nor depositing their energy primarily in ambient air. Bernstein et al. (Reference 3-6) have found that for electron beam experiments conducted in a large vacuum tank environment (that simulates the pressure and earth's magnetic field at altitudes between about 110 and 150 km) a beam plasma discharge (BPD) occurs when the beam current exceeds a certain critical value. After onset of the BPD, a large increase in the $3914\text{-}\overset{\circ}{\text{A}}$ intensity is observed to occur, accompanied by a large radial expansion of the beam profile to the point where single particle trajectory features disappear. The conditions required for onset of the BPD appear to be fulfilled in the EXCEDE experiments.

SECTION 4

SUMMARY, CONCLUSIONS, AND RECOMMENDATIONS

This report describes work performed to determine the adequacy of an electron energy-deposition code (which is based on single particle dynamics and is consistent with the theory inherent in nuclear predictive codes) to account for the magnitude and spatial distribution of energy deposition surrounding electron beams in space. For this purpose, comparisons were made between our code predictions and camera data relating to the PRECEDE II and EXCEDE:SPECTRAL experiments.

The PRECEDE II analysis involved a comparison between the size and shape of a video camera image of a pulse at an altitude of 102 km, recorded from the ground, and the calculated profile. Radiance values from the field data are not available for comparison. The EXCEDE:SPECTRAL work involved primarily a detailed comparison between the calculated and observed radiance (3914 Å) distribution, in the image plane of an on-board black and white camera, for a beam pulse at an altitude of 123 km. Secondly, it involved a comparison with preliminary photographic data recorded from the ground on a similar pulse.

In summary, the conclusions reached are as follows.

(1) The overall size and shape of the PRECEDE II image is reasonably consistent with the calculated size and shape based on contours of constant brightness. This comparison involved the gross dimensions of the pulse which are approximately 1.3 km along-the-field and 70 meters across-the-field. No high spatial-resolution or intensity comparisons can be made.

(2) For the EXCEDE:SPECTRAL image, the predicted radiance distribution is in gross disagreement with the reduced photographic data from the on-board camera, at least for the region within a few meters of the electron gun. In this region, the radiance data are as much as 2 orders-of-magnitude larger than the code prediction. This conclusion appears to be qualitatively supported by the preliminary ground-based photographic data, although a firm conclusion regarding this, and also the beam behavior farther from the gun, cannot be made until absolute intensities are assigned to these data.

It appears that there is something akin to the beam plasma discharge (BPD) phenomenon occurring in the EXCEDE:SPECTRAL experiment that serves to greatly enhance the emission rate of 3914-Å photons and to enlarge the beam, at least in the vicinity of the electron gun. Although the phenomenon is not well understood, it is believed that in a BPD additional ionization is produced through a cascade effect or discharge in which the plasma electrons are heated, possibly by cyclotron waves, to energies where they can ionize the ambient neutral gas to levels greatly exceeding those produced by the beam itself (Reference 3-6).

The secondary electron energy spectrum, under BPD conditions, is likely to be very different from that which exists for a normal beam, or under conditions following X-ray or beta-particle deposition in a nuclear environment. The implication is that certain conclusions drawn from spectral observations of spatial regions where a BPD is operating may not be applicable to the nuclear case. For example, the excitation rate of $N_2(v=1)$, leading to CO_2 vibraluminescence, may be quite different, relative to the 3914-Å emission rate, under BPD conditions than it is under "normal" conditions.

Even though BPD conditions may occur in a region near the electron gun, it is only reasonable to suppose that at some distance along the beam,

sufficiently far from the gun, the current of electrons drops to a sub-critical value where the BPD can no longer be maintained. Thereafter, the beam should behave in a "normal" manner. For EXCEDE diagnostic purposes, as well as for planning future EXCEDE experiments, it is very important to be able to distinguish between these regions.

To help clarify the applicability of present and future EXCEDE data for use in upgrading our nuclear (infrared) predictive codes, we make the following recommendations.

(1) Utilize available data and/or theory to confirm the presence of the BPD phenomenon in EXCEDE experiments. For example, from the available spectral data obtained in the EXCEDE:SPECTRAL experiment, determine the intensity ratios for selected lines and bands (including $5914 \text{ \AA}/1.5 \text{ \mu m}$) and compare them with corresponding ratios measured (or computed) for the aurora. Significant differences may be indicative of a BPD phenomenon in the electron beam.

(2) If BPD is confirmed, utilize all relevant data, together with applicable theory as necessary, in an attempt to delineate those spatial regions where the BPD and "normal" conditions apply.

(3) In planning future EXCEDE experiments, incorporate measurements from a platform sufficiently removed from the electron accelerator to permit an unobstructed view over a considerable length of the electron beam. In addition to reasons advanced elsewhere for such a stand-off platform, the possible presence of a BPD in the vicinity of the electron gun adds further impetus to this requirement.

REFERENCES

- 1-1. Archer, Douglas H., Requirements for Improved Infrared Prediction Capability: LWIR, MRC-R-583, Mission Research Corporation, October 1980.
- 2-1. Tarr, P. W., ARCTIC Code Electron Deposition Theory With Application to Project EXCEDE, HAES Report No. 10, DNA 3636T, MRC-R-173, Mission Research Corporation, 18 June 1975.
- 2-2. O'Neil, Robert R. (ed.) PRECEDE II: Summarized Results of An Artificial Auroral Experiment, HAES Report No. 77, AFGL-TR-78-0063, Air Force Geophysics Laboratory, 16 March 1978.
- 3-1. O'Neil, Robert R. (ed.) EXCEDE SPECTRAL Preliminary Results, AFGL-TM-41, Air Force Geophysics Laboratory 1980.
- 3-2. Kofsky, I. L., Photometrics, Inc., Private Communication, October 1980.
- 3-3. Grün, A. E., Z. Naturforsch., 129, 89 (1957).
- 3-4. Cohn, A., and G. Caledonia, J. App. Phys. 41, 3767 (1970).
- 3-5. Walt, M., et al., "Penetration of Auroral Electrons into the Atmosphere," in Physics of the Magnetosphere, ed. Carovillano, McCloy and Radoski, Reidel Publishing Company 1968.
- 3-6. Bernstein, W., et al., "Further Laboratory Measurements of the Beam-Plasma Discharge," J. Geophys. Res. 84, 7271 (1979).
- 3-7. Boquist, W. P., Technology International Corporation, Private Communication, June 1980.

DISTRIBUTION LIST

DEPARTMENT OF DEFENSE

Assistant Secretary of Defense
Comm, Cmd, Cont & Intell
ATTN: Dir of Intelligence Sys, J. Babcock

Assistant to the Secretary of Defense
Atomic Energy
ATTN: Executive Assistant

Command & Control Technical Center
ATTN: C-312, R. Mason
ATTN: C-650, G. Jones
3 cy ATTN: C-650, W. Heidig

Defense Communications Agency
ATTN: Code 101B
ATTN: Code 480
ATTN: Code 810, J. Barna
ATTN: Code 205
ATTN: Code 480, F. Dieter

Defense Communications Engineer Center
ATTN: Code R123
ATTN: Code R410, N. Jones

Defense Intelligence Agency
ATTN: DB, A. Wise
ATTN: DB-4C, E. O'Farrell
ATTN: DC-7D, W. Wittig
ATTN: DT-5
ATTN: DT-1B
ATTN: HQ-TR, J. Stewart

Defense Nuclear Agency
ATTN: NAFD
ATTN: NATD
ATTN: STNA
ATTN: RAE
3 cy ATTN: RAAE
4 cy ATTN: TITL

Defense Technical Information Center
12 cy ATTN: DD

Field Command
Defense Nuclear Agency
ATTN: FCPR

Field Command
Defense Nuclear Agency
Livermore Branch
ATTN: FCPRL

Interservice Nuclear Weapons School
ATTN: TTV

Joint Chiefs of Staff
ATTN: C3S, Evaluation Office
ATTN: C3S

Joint Strat Tgt Planning Staff
ATTN: JLA
ATTN: JLTW-2

DEPARTMENT OF DEFENSE (Continued)

National Security Agency
ATTN: B-3, F. Leonard
ATTN: W-32, O. Bartlett
ATTN: R-52, J. Skillman

Under Secretary of Def for Rsch & Engrg
ATTN: Strategic & Space Sys (OS)

WWMCCS System Engineering Org
ATTN: J. Hoff

DEPARTMENT OF THE ARMY

Assistant Chief of Staff for Automation & Comm
Department of the Army
ATTN: DAAC-ZT, P. Kenny

Atmospheric Sciences Laboratory
U.S. Army Electronics R&D Command
ATTN: DELAS-EO, F. Niles

BMD Advanced Technology Center
Department of the Army
ATTN: ATC-T, M. Capps
ATTN: ATC-O, W. Davies

BMD Systems Command
Department of the Army
2 cy ATTN: BMDSC-HW

Deputy Chief of Staff for Ops & Plans
Department of the Army
ATTN: DAMO-RQC

Electronics Tech & Devices Lab
U.S. Army Electronics R&D Command
ATTN: DELET-ER, H. Bomke

Harry Diamond Laboratories
Department of the Army
ATTN: DELHD-N-P, F. Wimenitz
ATTN: DELHD-I-TL, M. Weiner
ATTN: DELHD-N-RB, R. Williams
ATTN: DELHD-N-P

U.S. Army Comm-Elec Engrg Instal Agency
ATTN: CCC-EMEO-PED, G. Lane
ATTN: CCC-CED-CCO, W. Neuendorf

U.S. Army Communications Command
ATTN: CC-OPS-WR, H. Wilson
ATTN: CC-OPS-W

U.S. Army Communications R&D Command
ATTN: DRDCO-COM-RY, W. Kesselman

U.S. Army Foreign Science & Tech Ctr
ATTN: DRXST-SD

U.S. Army Materiel Dev & Readiness Cmd
ATTN: DRCLDC, J. Bender

DEPARTMENT OF THE ARMY (Continued)

U.S. Army Missile Intelligence Agency
ATTN: J. Gamble

U.S. Army Nuclear & Chemical Agency
ATTN: Library

U.S. Army Satellite Comm Agency
ATTN: Document Control

U.S. Army TRADOC Sys Analysis Actvy
ATTN: ATAA-TDC
ATTN: ATAA-PL
ATTN: ATAA-TCC, F. Payan, Jr

DEPARTMENT OF THE NAVY

Joint Cruise Missiles Project Ofc
Department of the Navy
ATTN: JCMG-707

Naval Air Development Center
ATTN: Code 6091, M. Setz

Naval Air Systems Command
ATTN: PMA 271

Naval Electronic Systems Command
ATTN: PME 106-13, T. Griffin
ATTN: PME 117-2013, G. Burnhart
ATTN: PME 117-211, B. Kruger
ATTN: Code 501A
ATTN: PME 106-4, S. Kearney
ATTN: Code 3101, T. Hughes
ATTN: PME 117-20

Naval Intelligence Support Ctr
ATTN: NISC-50

Naval Ocean Systems Center
ATTN: Code 5322, M. Paulson
ATTN: Code 532, J. Bickel
3 cy ATTN: Code 5324, W. Moler
3 cy ATTN: Code 5323, J. Ferguson

Naval Research Laboratory
ATTN: Code 7500, B. Wald
ATTN: Code 4700, T. Coffey
ATTN: Code 7550, J. Davis
ATTN: Code 4780, S. Ossakow
ATTN: Code 7950, J. Goodman
ATTN: Code 4187

Naval Space Surveillance System
ATTN: J. Burton

Naval Surface Weapons Center
ATTN: Code F31

Naval Telecommunications Command
ATTN: Code 341

Office of Naval Research
ATTN: Code 420
ATTN: Code 465
ATTN: Code 421

DEPARTMENT OF THE NAVY (Continued)

Office of the Chief of Naval Operations
ATTN: OP 65
ATTN: OP 981N
ATTN: OP 941D

Strategic Systems Project Office
Department of the Navy
ATTN: NSP-2722, F. Wimberly
ATTN: NSP-2141
ATTN: NSP-43

DEPARTMENT OF THE AIR FORCE

Aerospace Defense Command
Department of the Air Force
ATTN: DC, T. Long

Air Force Geophysics Laboratory
ATTN: OPR, H. Gardiner
ATTN: OPR-1
ATTN: LKB, K. Champion
ATTN: OPR, A. Stair
ATTN: S. Basu
ATTN: PHP
ATTN: PHI, J. Buchau
ATTN: R. Thompson

Air Force Weapons Laboratory
Air Force Systems Command
ATTN: SUL
ATTN: NTYC
ATTN: NTN

Air Force Wright Aeronautical Lab
ATTN: W. Hunt
ATTN: A. Johnson

Air Logistics Command
Department of the Air Force
ATTN: OO-ALC/MM, R. Blackburn

Air University Library
Department of the Air Force
ATTN: AUL-LSE

Air Weather Service, MAC
Department of the Air force
ATTN: DNXF, R. Babcock

Assistant Chief of Staff
Intelligence
Department of the Air Force
ATTN: INED

Assistant Chief of Staff
Studies & Analyses
Department of the Air Force
ATTN: AF/SASC, C. Rightmeyer
ATTN: AF/SASC, W. Keaus

Ballistic Missile Office
Air Force Systems Command
ATTN: MNXKH, J. Allen

DEPARTMENT OF THE AIR FORCE (Continued)

Deputy Chief of Staff
Operations Plans and Readiness
Department of the Air Force
ATTN: AFXOKT
ATTN: AFXOKCD
ATTN: AFXOKS
ATTN: AFXOXFD

Deputy Chief of Staff
Research, Development, & Acq
Department of the Air Force
ATTN: AFRDSP
ATTN: AFRDS
ATTN: AFRDSS

Electronic Systems Division
Department of the Air Force
ATTN: DCKC, J. Clark

Electronic Systems Division
Department of the Air Force
ATTN: XRW, J. Deas

Electronic Systems Division
Department of the Air Force
ATTN: YSEA
ATTN: YSM, J. Kobelski

Foreign Technology Division
Air Force Systems Command
ATTN: NIIS Library
ATTN: TQTD, B. Ballard

Headquarters Space Division
Air Force Systems Command
ATTN: SKY, C. Kennedy
ATTN: SKA, D. Bolin

Headquarters Space Division
Air Force Systems Command
ATTN: YZJ, W. Mercer

Headquarters Space Division
Air Force Systems Command
ATTN: E. Butt

Rome Air Development Center
Air Force Systems Command
ATTN: TSLD
ATTN: OCS, V. Coyne

Rome Air Development Center
Air Force Systems Command
ATTN: EEP

Strategic Air Command
Department of the Air Force
ATTN: XPFS
ATTN: DCXT
ATTN: NRT
ATTN: DCXR, T. Jorgensen
ATTN: DCX

OTHER GOVERNMENT AGENCIES

Central Intelligence Agency
ATTN: OSWR/NED

OTHER GOVERNMENT AGENCIES (Continued)

Department of Commerce
National Bureau of Standards
ATTN: Sec Ofc for R. Moore

Department of Commerce
National Oceanic & Atmospheric Admin
ATTN: R. Grubb

Institute for Telecommunications Sciences
National Telecommunications & Info Admin
ATTN: A. Jean
ATTN: L. Berry
ATTN: W. Utlaug

U.S. Coast Guard
Department of Transportation
ATTN: G-DOE-3/TP54, B. Romine

DEPARTMENT OF ENERGY CONTRACTORS

EG&G, Inc
Los Alamos Division
ATTN: J. Colvin
ATTN: D. Wright

Lawrence Livermore National Lab
ATTN: L-31, R. Hager
ATTN: Technical Info Dept Library
ATTN: L-389, R. Ott

Los Alamos National Scientific Lab
ATTN: D. Simons
ATTN: E. Jones
ATTN: D. Westervelt
ATTN: P. Keaton
ATTN: MS 670, J. Hopkins
ATTN: R. Taschek
ATTN: MS 664, J. Zinn

Sandia National Laboratories
Livermore Laboratory
ATTN: T. Cook
ATTN: D. Murphey

Sandia National Lab
ATTN: Space Project Div
ATTN: D. Dahlgren
ATTN: ORG 1250, W. Brown
ATTN: ORG 4241, T. Wright
ATTN: 3141
ATTN: D. Thornbrough

DEPARTMENT OF DEFENSE CONTRACTORS

Aerospace Corp
ATTN: N. Stockwell
ATTN: V. Josephson
ATTN: R. Slaughter
ATTN: D. Olsen
ATTN: I. Garfunkel
ATTN: T. Salmi
ATTN: J. Straus
ATTN: S. Bower

Analytical Systems Engineering Corp
ATTN: Radio Sciences

DEPARTMENT OF DEFENSE CONTRACTORS (Continued)

University of Alaska
ATTN: N. Brown
ATTN: T. Davis
ATTN: Technical Library

Analytical Systems Engineering Corp
ATTN: Security

Barry Research Corporation
ATTN: J. McLaughlin

BDM Corp
ATTN: T. Neighbors
ATTN: L. Jacobs

Berkeley Research Associates, Inc
ATTN: J. Workman

BETAC
ATTN: J. Hirsch

Boeing Co
ATTN: S. Tashird
ATTN: G. Hall
ATTN: M/S 42-33, J. Kennedy

Booz-Allen & Hamilton, Inc
ATTN: B. Wilkinson

University of California at San Diego
ATTN: H. Booker

Charles Stark Draper Lab, Inc
ATTN: D. Cox
ATTN: J. Gilmore

Communications Satellite Corp
ATTN: D. Fang

COMSAT Labs
ATTN: G. Hyde
ATTN: R. Taur

Cornell University
ATTN: M. Kelly
ATTN: D. Farley, Jr

Electrospace Systems, Inc
ATTN: H. Logston

ESL, Inc
ATTN: J. Marshall

General Electric Co
ATTN: M. Bortner
ATTN: A. Hancar

General Electric Co
ATTN: C. Zierdt
ATTN: A. Steinmayer

General Electric Co
ATTN: F. Reibert

General Electric Tech Services Co, Inc
ATTN: G. Millman

General Research Corp
ATTN: J. Garbarino
ATTN: J. Ise, Jr

DEPARTMENT OF DEFENSE CONTRACTORS (Continued)

Horizons Technology, Inc
ATTN: R. Kruger

HSS, Inc
ATTN: D. Hansen

IBM Corp
ATTN: F. Ricci

University of Illinois
ATTN: Security Supervisor for K. Yeh

Institute for Defense Analyses
ATTN: J. Bengston
ATTN: J. Aein
ATTN: E. Bauer
ATTN: H. Wolfhard

International Tel & Telegraph Corp
ATTN: G. Wetmore
ATTN: Technical Library

JAYCOR
ATTN: J. Sperling

JAYCOR
ATTN: J. Doncarlos

Johns Hopkins University
ATTN: T. Potemra
ATTN: J. Phillips
ATTN: T. Evans
ATTN: J. Newland
ATTN: P. Komiske

Kaman TEMPO
ATTN: W. McNamara
ATTN: T. Stephens
ATTN: M. Stanton
ATTN: W. Knapp
ATTN: DASIAC

Linkabit Corp
ATTN: I. Jacobs

Litton Systems, Inc
ATTN: R. Grasty

Lockheed Missiles & Space Co, Inc
ATTN: R. Johnson
ATTN: M. Walt
ATTN: W. Imhof

Lockheed Missiles & Space Co, Inc
ATTN: Dept 60-12
ATTN: D. Churchill

M.I.T. Lincoln Lab
ATTN: D. Towle
ATTN: L. Loughlin

Martin Marietta Corp
ATTN: R. Heffner

Meteor Communications Consultants
ATTN: R. Leader

DEPARTMENT OF DEFENSE CONTRACTORS (Continued)

McDonnell Douglas Corp
ATTN: W. Olson
ATTN: G. Mroz
ATTN: R. Halprin
ATTN: J. Moule
ATTN: N. Harris

Mission Research Corp
ATTN: R. Hendrick
ATTN: F. Fajen
ATTN: D. Sappenfield
ATTN: Tech Library
ATTN: R. Kilb
ATTN: S. Gutsche
ATTN: R. Bogusch
4 cy ATTN: D. Archer
5 cy ATTN: Document Control

Mitre Corp
ATTN: B. Adams
ATTN: A. Kymmel
ATTN: G. Harding
ATTN: C. Callahan

Mitre Corp
ATTN: W. Foster
ATTN: J. Wheeler
ATTN: M. Horrocks
ATTN: W. Hall

Pacific-Sierra Research Corp
ATTN: F. Thomas
ATTN: E. Field, Jr
ATTN: H. Brode

Pennsylvania State University
ATTN: Ionospheric Research Lab

Photometrics, Inc
ATTN: I. Kofsky

Physical Dynamics, Inc
ATTN: E. Fremouw

R & D Associates
ATTN: W. Karzas
ATTN: F. Gilmore
ATTN: B. Gabbard
ATTN: M. Gantsweg
ATTN: C. Greifinger
ATTN: W. Wright
ATTN: R. Turco
ATTN: H. Ory
ATTN: R. Lelevier
ATTN: P. Haas

R & D Associates
ATTN: L. Delaney
ATTN: B. Yoon

Rand Corp
ATTN: E. Bedrozian
ATTN: C. Crain

Riverside Research Institute
ATTN: V. Trapani

Rockwell International Corp
ATTN: R. Buckner

DEPARTMENT OF DEFENSE CONTRACTORS (Continued)

Rockwell International Corp
ATTN: S. Quilici

Santa Fe Corp
ATTN: D. Paolucci

Science Applications, Inc
ATTN: E. Straker
ATTN: D. Hamlin
ATTN: L. Linson
ATTN: C. Smith

Science Applications, Inc
ATTN: SZ

Science Applications, Inc
ATTN: J. Cockayne

SRI International
ATTN: G. Smith
ATTN: W. Jaye
ATTN: D. Neilson
ATTN: A. Burns
ATTN: G. Price
ATTN: R. Tsunoda
ATTN: R. Livingston
ATTN: W. Chesnut
ATTN: J. Petrickes
ATTN: R. Leadabrand
ATTN: C. Rino
ATTN: M. Baron

Sylvania Systems Group
ATTN: M. Cross

Technology International Corp
ATTN: W. Boquist

Tri-Com, Inc
ATTN: D. Murray

TRW Defense & Space Sys Group
ATTN: R. Plebuch
ATTN: D. Dee

Utah State University
ATTN: K. Baker
ATTN: J. Dupnik
ATTN: L. Jensen

Visidyne, Inc
ATTN: J. Carpenter
ATTN: C. Humphrey

DATE
FILMED
-8